Unraveling the Effects of Morphology at the Core/Shell Interface of InP-based Quantum Dots

By

Sophia Michelle Click

Dissertation

Submitted to the Faculty of the

Graduate School of Vanderbilt University

in partial fulfillment of the requirements

for the degree of

DOCTOR OF PHILOSOPHY

in

Chemistry

May 12, 2023

Nashville, Tennessee

Approved:

Sandra J. Rosenthal, Ph.D.

Janet E. Macdonald, Ph.D.

Lauren E. Buchanan, Ph.D.

Richard F. Haglund, Ph.D.

For my goddaughter,
Mariana Sophia

May this grain of knowledge
contribute to a world that inspires you.

Acknowledgements

I would like to thank my advisor, Dr. Sandra Rosenthal for allowing me the freedom to make my own mistakes and for having faith that I could find my way through them. I would also like to thank my committee members, Dr. Lauren Buchanan, Dr. Janet Macdonald, and Dr. Richard Haglund, for their mentorship and wise counsel over the course of my studies.

Completion of the work contained within this dissertation was accomplished with the support of research professors James McBride, Oleg Kovtun, and Ian Tomlinson, fellow Rosenthal lab members, Laurel Bellocchio, Sebastian Flores, Ruben Torres, Dr. Cara Bradsher, Dr. Nathaniel Freymeyer, Dr. Talitha VanWie, Dr. Lucas Thal, Dr. Danielle Bailey, and Dr. Kemar Reid, and research collaborators Dr. Christopher Stachurski, Dr. Madeleine Fort, Dr. Matthew Chisholm, and Alexandra Koziel. This work was supported by grants from the National Science Foundation (CHE-1506587), the Vanderbilt Institute of Nanoscale Science and Engineering, the Vanderbilt Graduate School, and the Vanderbilt Chemistry Department.

To James McBride-thank you for reading all my early drafts and giving me your honest feedback, despite my begrudging acceptance of your critiques. Your advice has made me a better scientist.

To my friends and family, your unwavering support has buoyed me through this journey. Thank you for your steadfast love.

TABLE OF CONTENTS

Commented [CSM1]: Table of Contents

List of Tables

Table Page

List of Figures

CHAPTER I: INTRODUCTION

Commented [CSM2]: CHAPTER I: Introduction

1.1 Colloidal Semiconductor Nanocrystals

Colloidal quantum dots (QDs) are nanocrystals made of semiconductors such as InP or CdSe that experience quantum confinement due to their small size.[1] Quantum confinement occurs when a semiconductor nanocrystal becomes smaller than its Bohr exciton diameter, causing the electrons to be confined by the edge of the nanocrystal. This confinement causes the QD's photophysical and electronic properties to become size-dependent, making QDs uniquely capable of bright, color-pure fluorescence that can be precisely controlled by their size and crystalline structure.[2–4] Since their discovery nearly 40 years ago, fluorescent QDs have been optimized as emitters in a wide array of areas including biomedical imaging[5,6], lasing[7–9], lighting displays [10–14] , and photonic quantum technology.[15] Currently, they have been best implemented as competitive alternatives to organic fluorophores in QD-based LEDs (QLEDs) with high external quantum efficiencies (EQE), high color saturation, and low-cost solution processing.[16]

Quantum-confined semiconductor clusters were first theorized by Dr. Louis E. Brus in the early 1980s-a theory that was quickly proven with the synthesis of quantum-confined CdS clusters and a variety of other colloidal semiconductor clusters.[1,2,17–22] In 1984, Brus modeled the effect of quantum confinement on band gap as the dependence of the energy of the lowest excited state on:[2]

$$E_{ex} = \frac{\hbar^2\pi^2}{2r^2}\left(\frac{1}{m_e}+\frac{1}{m_h}\right) - \frac{1.8e^2}{\varepsilon_2 r} + \frac{e^2}{R}\overline{\sum_{n=1}^{\infty}\alpha_n\left(\frac{S}{r}\right)^{2n}}$$

in which the bar in the third term means average over the first wavefunction for a particle in a sphere, $\hbar$ is the reduced Planck's constant, r is the radius of the nanocrystal, m_e and m_h are the effective masses of the electron and hole respectively, e is the absolute charge of an electron, ε_2 is the dielectric constant of the semiconductor material, α_n is a constant that relates the dielectric

constants of the semiconductor material and the surrounding medium, and S is the wavefunction that describes the position of the electron and hole in the 1S exciton. The first term in this equation is the quantum energy of localization and describes the energy of the electron-hole pair spacing similar to Schrodinger's particle-in-a-box, where the electron-hole energetic spacing is inversely related to the widening of the band gap. The second term describes the coulombic attraction of the charge carriers, and the third term describes the solvation energy loss.

By 1990, the term "Quantum Dots" was coined and soon thereafter indium phosphide joined the newly established field.[23,24] To date, the highest performing QDs are CdSe-based but inherent cadmium toxicity as a heavy-metal limits their implementation in biological and industrial applications.[25,26] Indium phosphide offers an alternative QD system that exhibits size-tunable fluorescence throughout the visible and lower IR spectrum.[27,28] Although InP-based QDs have successfully been implemented in commercialized products, such as Samsung's line of QLED televisions, their photostability and synthetic control still does not match that of their CdSe-based counterparts.[14] If InP QDs are to see continued success as visible fluorophores, further research must be done to overcome the challenges that limit them from performing at the same rigorous level as Cd-based QDs.

Bulk InP has a smaller but similarly placed bandgap relative to bulk CdSe (1.27 vs 1.74 eV), that allows for InP QD emission to be tuned throughout the visible and into the lower infrared (IR) region. Additionally, InP higher covalency leads to a higher carrier mobility (4600 vs 900 cm^2/Vs) and a significantly larger Bohr exciton diameter than CdSe (216.1 vs 60.4 Å), thus offering greater optical tunability than CdSe.[29] Despite these advantages, indium phosphide's higher covalency has stymied synthetic progress by requiring more reactive precursors to form the lattice and producing nanocrystals that are more prone to lattice defects.[30] This has resulted in an unexplained growth

barrier and a heightened sensitivity to oxidative degradation. Additionally, years of incomplete or unsuccessful epitaxial shelling with ZnS yielded QDs that could not compete with Cd-based QDs.[31] Since the discovery that ZnSe can grow a thick intermediary shell because of its reduced lattice mismatch with InP, the field has seen significant improvements in the photophysical properties of InP-based QDs with photoluminescent quantum yields (PLQYs) greater than 95%, emission linewidths (fwhm) down to 35 nm, and QLEDS with external quantum efficiencies >20%.[14,32–35]

1.2 Indium Phosphide Quantum Dots

In their most general format, solution-based InP nanocrystal syntheses involve the reaction of indium and phosphorus sources at high temperatures (>180 °C) in a high-boiling point solvent in the presence of a stabilizing ligand. Chen et al.[36] and Tamang et al.[37] have eloquently discussed these chemistries. The most common chemistries are briefly summarized and listed in Table 1.1.

1.2.1 Synthesis

There are a variety of indium sources used, ranging from long alkyl-chain carboxylates such as indium myristate[38], indium palmitate[39], indium stearate[40], indium laurate,[41] and indium oleate[42] to indium halides[43,44] and indium amidinates[45]. Indium carboxylate chemistry has been optimized to control sample size distribution and serves a dual role as stabilizing ligand on the QD's surface, but carboxylates can also participate in unwanted side reactions that create oxidative conditions during QD growth. It should be noted that long-chain indium carboxylates are often formed *in situ* from indium acetate and the desired carboxylic acid as the first step of the reaction, without monitoring for the complete displacement of acetate.[46] This uncertainty may affect the reproducibility of these syntheses. Indium halides and amides avoid these pitfalls but require additional ligand sources and their newer chemistries are not as well defined. Almost at odds with

this variety, there are very few phosphorous sources that are reactive enough for InP QD synthesis. For over 30 years tris(trimethylsilyl)phosphine (TMSiP) has been the dominant phosphorus source used in InP reactions [35,47,48]. A recent push to find a less pyrophoric phosphorus source has led to the use of aminophosphines. [49,50] Aminophosphine precursors can be tailored to be less reactive than TMSiP, tuning their conversion reactivity over a wide range that allows for precursor conversion limited growth at high temperatures.[51] Attempts to use Zn_3P_2, PCl_3, phosphine gas generated from calcium phosphide, white phosphorus, sodium phosphaethynolate, and analogues of TMSiP have been performed with limited success.[52–59] The addition of ligand sources such as zinc halides[60,61], zinc carboxylates[33,62], amines (oleylamine[63], trioctylamine[42], hexadecylamine[45]), trioctlyphosphine (TOP)[40], or phenylacetic acid[64] are used to passivate and solubilize the QDs. Octadecene (ODE) is the most common solvent in these reactions, while oleylamine is used with aminophosphines as ligand, solvent, and activator.[43,51] Other non-coordinating solvents that have been implemented include toluene[65], mesitylene[45], and decane[39]. Purification of QDs is usually done via centrifugation with polar 'anti'-solvents such as acetone, ethanol, acetonitrile, and isopropanol, but recent work utilizing gel permeation chromatography provides an alternate method that size-selects without stripping ligands.[66,67]

Nguyen et al. recently used machine learning models comparing over 200 published InP QD syntheses to investigate trends in InP syntheses and found that annealing temperature, annealing time, and the presence of zinc additives were the most influential parameters studied when predicting optical peaks and nanocrystal size.[68] The first two make sense considering the significant role annealing temperature and time play in nucleation and growth kinetics. The role of zinc additives is discussed in detail later in this review.

Table 1.1 Common chemicals and synthetic techniques used in recent InP QD syntheses.

Indium Precursor	Phosphorus Precursor	Ligand Source	Solvent	Synthetic Technique
Acetate (2-C)	Tris(trimethylsilyl)phosphine	In-carboxylates	Octadecene	Hot Injection
Laurate (12-C)	Tris(trimethylgermanyl)phosphine	Zn-carboxylates	Oleylamine	Heat-up
Myristate (14-C)	Tris(tert-butyldimethylsilyl)phosphine	Oleylamine	Toluene	Microwave
Palmitate (16-C)	Triarylsilylphosphines	Trioctylamine	Mesitylene	Clusters
Stearate (18-C)	Tris(diethylamino)phosphine	Hexadecylamine	Decane	Continuous injection
Oleate (18-C)	Tris(dimethylamino)phosphine	In-halides		
Fluoride	Zinc Phosphide	Zn-halides		
Chloride	Phosphorus Trichloride	Trioctylphosphine		Experimental Abundance
Bromide	Phosphine gas (*in situ*)	Phenylacetic acid		>40%
Iodide	White Phosphorus			10-40%
Amidinates	Sodium Phosphaethynolate			<10%

InP syntheses usually fall into one of four categories: heat-up,[69] microwave,[39] hot injection,[35] or continuous injection.[70] The first published synthesis of crystalline, colloidally stable InP QDs by Micic et al.[23] utilized the heat-up technique by annealing a chloroindium oxalate complex, TMSiP in trioctylphosphine oxide (TOPO), and TOP at 270 °C for several days. Since then, noncoordinating solvents like ODE have replaced TOPO and TOP, allowing QDs to be grown in minutes instead of days.[48] Microwave syntheses rapidly heat precursors, decreasing growth time to seconds, but often at the cost of sample homogeneity.[39,71] Because of this, most syntheses have moved away from heat-up methods to a hot injection of TMSiP into the heated indium carboxylate solution. With the discovery of InP clusters as a reaction intermediate, some syntheses have opted to react In and P precursors at lower temperatures (<120°C) to form InP clusters and then hot inject these clusters as single-source precursors into indium solutions at high temperatures (>200°C) for growth.[72,73] All of these methods can grow InP QDs up to 3.5 nm in diameter, but require secondary injections of In/P precursors at annealing temperatures to grow larger (>4 nm) InP QDs.[14,40,62,69,74] Achorn et al. utilized a continuous injection method for nucleation and growth where TMSiP was continuously injected into a solution containing excess indium oleate at 300°C. As the QDs grew

larger the rate of injection was slowed to prefer growth over nucleation and caused size focusing as the QDs grew larger. This approach has overcome the size barrier in InP syntheses and decreased the size distribution of the produced QDs (27 nm or 81 meV absorbance peak half width at half maximum, HWHM).[70]

1.2.2 Shape Control

Until recently, shape control of InP QDs was limited to addressing overall size and distribution of small (<5 nm diameter), spherical nanocrystals via synthetic parameters such as annealing temperature and time, precursor reactivity and concentration, ligand type, and zinc presence.[49,60,75] The recent emergence of tetrahedral InP QDs is the first demonstration that faceted InP nanocrystal shape can be controlled *in situ*. In 2016, Kim et al. produced 5-10 nm tetrahedral and triangular prism InP QDs.[76] (Figure 1.1a) These QDs were halide-amine co-passivated and consisted of a zinc blende lattice with indium-rich (111) facets. The authors attribute shape control to an acid-free synthesis that uses oxygen-free precursors instead of the more traditional carboxylic acids to avoid in-situ oxidation. It may be that previous acid-free InP syntheses did not produce tetrahedral InP because they did not grow large enough to exhibit faceting.[49,60] Interestingly, the authors note that these structures exhibit a higher energy first exciton peak than similarly sized spherical InP QDs, indicating increased electron confinement. Since spheres with diameter, *d*, contain more than 4 times the volume of tetrahedrons with the same edge length, *d*, InP QD samples with the same diameter and edge lengths should not be assumed to be the same size, especially when using sizing curves that assume spherical shape.

In 2018, Stein et al. compared this acid-free synthesis with two other synthetic techniques, both utilizing carboxylic acids, and also found that the acid-free synthesis produced tetrahedral InP QDs. X-ray emission spectroscopy (XES) found oxidized phosphorus in all three samples but

noted that the oxidized phosphorus in the tetrahedral sample was in the form of electrostatically interacting phosphonium byproducts instead of oxidized surface PO_x present in the other two samples.[77] Since then tetrahedral InP QDs have also been produced using syntheses containing carboxylic acids, calling into question the requirement for oxide-free surfaces to grow tetrahedrons. These syntheses were able to grow >5 nm tetrahedral InP QDs via slow secondary injections with an indium precursor that was made more reactive by the addition of either zinc carboxylates or trioctylphosphine.[40,74]

Most recently, InP tetrapods have been isolated as metastable intermediates in the formation of tetrahedral InP QDs.[78] (Figure 1.1b) By reducing the reaction temperatures to 170 °C and adding a strong base to accelerate the initial precursor conversion rate, Kim et al. were able to suppress growth on the nucleated tetrapods, producing tetrapods with 5-15 nm arms and a 92% shape yield. These tetrapods exhibited simultaneous emission from up to 4 sites due to their quasi-2D confinement and the multiexcitons interacted in a correlated, coherent fashion.[79] Moving forward with these lessons learned, the library of InP QD shapes may be expanded to include anisotropic morphologies such as rods and more complex heterostructures such as shelled or tipped tetrapods.

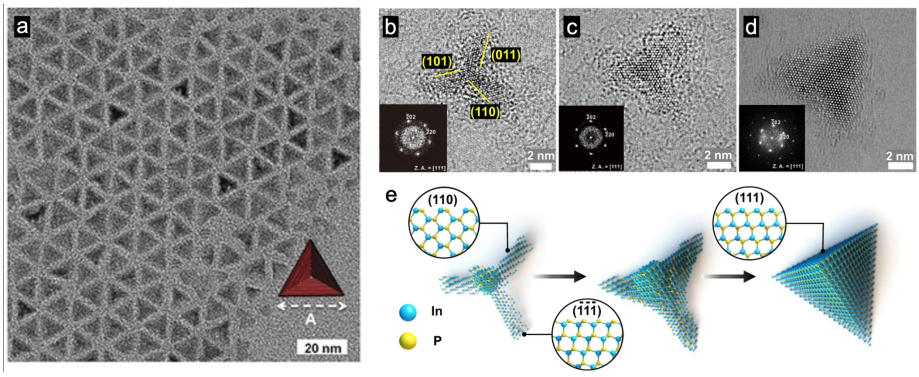

Figure 1.1 (a) TEM image of InP tetrahedrons synthesized at 300 °C in acid-free conditions. (b-d) HR-TEM images of InP nanostructures found during growth from tetrapod to tetrahedron and (e) schematic illustrations of the crystalline structures. Reproduced from ref. [76] and ref. [78] with permission from John Wiley and Sons and Springer Nature.

1.2.3 Classical Growth Mechanisms

Quantum dot formation is generally assumed to follow two steps: nucleation of seed crystals from monomeric precursors and then growth of seeds via adsorption of further monomers or aggregation of seed crystals. The nucleation step of this model is based on Becker and Doring's Classical Nucleation Theory (CNT) developed in the 1930's to describe the thermodynamics of phase transitions.[80,81] By weighing the favorability of bonding (bulk free energy) against the surface energy of nuclei at increasing sizes, the model calculates a critical radius above which it is thermodynamically favorable for the nucleus to grow and below which it is more favorable for the nucleus to redissolve back into monomer species (Figure 1.2a). CNT describes nucleation but does not describe growth mechanisms on formed nuclei. In the 1950's LaMer adapted CNT specifically to describe nanocrystal nucleation and growth. The LaMer model assumes that the nucleation and growth steps can be separated during synthesis by rapidly increasing the concentration of monomers to induce a 'burst' of nucleation events that quickly depletes the monomer concentration to favor growth over nucleation (Figure 1.2b). Growth, according to this model, occurs via diffusion-limited adsorption of monomers on nuclei. In other systems, such as CdSe QDs, these models work well to describe nucleation and growth. Further studies by Peng et al. found focusing and defocusing growth regimes that could be controlled by monomer concentration to produce CdSe samples with high morphological uniformity.[4] Unfortunately, InP QDs have been

shown to deviate significantly from classical models, which may explain struggles with size tunability and broad emission linewidths.

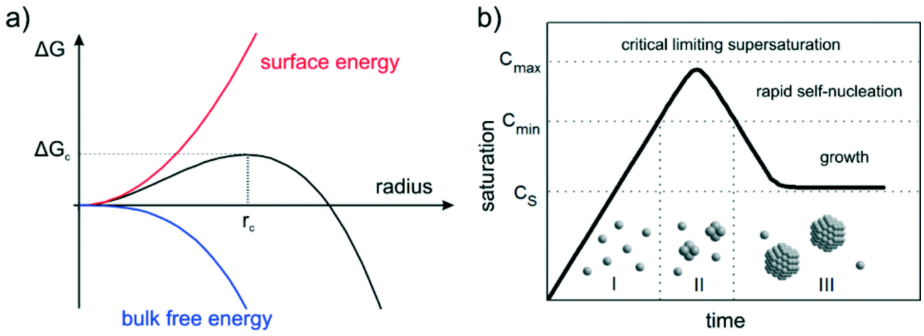

Figure 1.2 (a) Classical nucleation theory model of how surface area and bulk free energy change with increasing particle size to determine the critical radius size (r_c) for nucleation. (b) LaMer model of concentration regimes that favor nucleation vs growth of nanoparticles. Reproduced from ref. [80] with permission from the Royal Society of Chemistry.

1.2.4 Cluster Formation

The first significant deviation from classical theory is the ability for InP to form kinetically stable sub-nanometer clusters. InP cluster formation was first shown by Xie et al. in 2009 from the consistent appearance of an absorbance feature at 386 nm. Concentration and temperature variations yielded the same feature, indicating ~1 nm "magic-sized" clusters (MSCs). In 2016, the first direct measurements of the clusters came from MALDI-TOF mass spectrometry of InP growth solutions, revealing 10 kDa clusters and the first single-crystal X-ray diffraction patterns (XRD) of the InP MSCs.[38,82] This evidence directly contradicts CNT, since these clusters are much smaller than the calculated critical radius of InP nuclei. In 2015, Gary et al. found that the same clusters acted as intermediates in the formation of InP QDs and proposed a two-step nucleation model with the MSCs as kinetically persistent, isolable intermediates where the second nucleation event,

which could be induced with only MSCs as single-source precursors, was still described using the LaMer mechanism of nucleation and growth.[72] There are three likely mechanisms for QD formation involving nanoclusters: homogenous growth where clusters continuously grow, monomer-driven growth where clusters dissolve into monomers used to grow, and cluster assembly where clusters aggregate.[83] Since the single-crystal XRD of the InP MSCs revealed that the clusters have a pseudo-tetrahedral arrangement that is markedly different from the zinc blende crystalline phase of the produced InP QDs, homogenous growth and templated growth are unlikely mechanisms. Furthermore, varying the concentration of clusters used during QD synthesis indicated a first-order rate law, ruling out a rate-limiting cluster aggregation step.[84] It is more likely that the clusters either partially or fully dissolve to produce monomers or fragments for growth. A ^{13}C NMR study of MSC ligand dynamics found that at room temperature both exogenous acid and indium carboxylate ligands nonselectively incorporate onto the clusters' surface.[84] This suggests an acid-induced exchange as the first step of cluster dissociation and further supports the helpful role of excess indium carboxylate during QD growth.[84] Thus far, the extent of dissolution and the identities of produced monomers/fragments have not been determined.

1.2.5 Size-Dependent Growth Rate

Including cluster formation as an additional step toward nucleation and growth still does not fully account for the variation of InP QDs from the LaMer model. Even when using clusters as a single-source precursor, syntheses still struggle to separate nucleation from growth. It has been noted that InP clusters persist, even at high temperatures, well into the reactions.[38] Analysis of absorption changes over the course of the reaction indicates that nucleation also persists beyond the LaMer-like burst of several seconds.[51] By using an array of aminophosphines with different conversion reactivities, McMurtry et al. accessed precursor conversion limited kinetics. With both

low (180 °C) and high (270 °C) temperatures, they found relatively slow, continuous nucleation concurrent with nanoparticle growth. Absorbance-based calculations of nanocrystal concentration throughout syntheses indicated that nucleation occurred during most of growth and was dependent on the temperature of the reaction.[51] At lower temperatures nucleation was continuous throughout the reaction, but at higher temperatures nucleation finished within the first 10% of the reaction. Yet the size distributions were similar for both. This could be explained by a size-dependent growth rate, where larger particles grow much more slowly than smaller ones. This mechanism appears to be determined by the kinetics of monomer attachment, rather than diffusion limitations. Achorn et al. also found nucleation, growth, and size focusing occurring continuously throughout their syntheses.[70] In their seedless continuous injection study, new QDs continuously nucleated while existing larger QDs grew until a point where their growth slowed significantly (as seen by the halt in red shifting of the lowest energy absorbance peak). Yet, during this process the size distribution (according to the hwhm of the absorbance peak) decreased steadily. As shown in Figure 1.3, this unexpected 'focusing' of the size distribution was explained as the growth of larger nanoparticles slowed enough that newly nucleated nanoparticles could quickly catch up. Thin shellings of the QDs revealed a smaller population, whose absorbance was likely masked by the larger population. By drastically decreasing the continuous injection rate after a rapid initial growth period, precursor concentrations became low enough to inhibit further nucleation events while still allowing for very slow growth and size focusing of the existing QDs. (Figure 1.3) After this slow second injection, thin shelling of the QDs showed a single, narrow PL peak indicative of one size population with a small size distribution.[70]

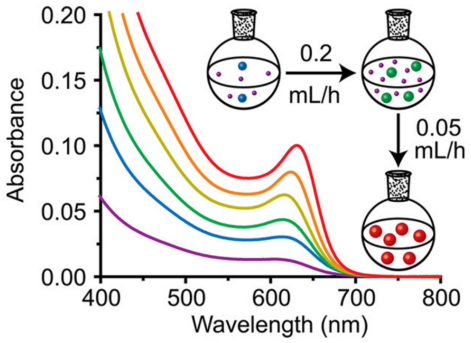

Figure 1.3. Absorption spectra of aliquots taken as variable-rate injections induce size-focused growth. Reprinted (adapted) with permission from ref [70]. Copyright 2020 American Chemical Society.

1.3 InP QD Surface Chemistry

Once formed, the surface chemistry of InP QDs is dictated by the ligands and bonding environment at the surface. Significant work studying the ligand exchange dynamics, the role of surface oxidation and mechanisms of in situ oxidation, the effects of surface fluorination, and control of Zn-In interface for shelling has opened the door for InP QDs to be engineered for a variety of applications.

1.3.1 Ligands

Long-chain saturated hydrocarbons with polar head groups are often used in nanoparticle synthesis as ligands that bind to the surface of the nanoparticles to solubilize them, passivate undercoordinated surface atoms, and control growth. For InP QDs common ligands used are fatty acid carboxylates bound to indium. An NMR study of InP QDs grown with indium palmitate in ODE found a coordination sphere of tightly bound carboxylates predominately chelating to indium with secondary bridging to indium or phosphorus.[85] This is typical of X-type binding and indicates

strong binding to the nanocrystal surface. In 2002, Battaglia et al. compared indium carboxylates with varying chain lengths (from 12 to 18-carbons with lauric, myristic, palmitic, and stearic acid) and found that myristate (14-carbon chain) and palmitate (16-carbon chain) produced the narrowest absorption linewidths. They also saw a dramatic influence of carboxylate concentration on the produced QDs. Using a 1:3 ratio of In:carboxylate produced the sharpest absorption features, while straying much lower (1:2) or higher (1:4.5) produced QDs without any distinguishable absorption peak.[48] Care should be taken in preparation of indium carboxylates as incomplete acetate displacement can affect reaction kinetics and improperly dried indium carboxylates can contain water that provides oxidative conditions during QD growth.[86,87]

Primary amines are another common ligand in nanoparticle synthesis that can control particle shape, affect precursor conversion kinetics, and donate protons. Additionally, when aminophosphines are used instead of TMSiP, primary amines are necessary to hydrolyze the aminophosphine into the more reactive species PH_3.[49] Amines significantly alter reaction kinetics and thermodynamics, although the mechanism by which they do this is still debated. In 2007, Xie et al. found that the addition of amine reduced the temperature required to form InP QDs and varying the concentration of amine present tuned the size of the produced QDs.[88] In 2010, Allen et al. monitored TMSiP depletion rates with NMR and found that amine addition slowed the depletion rate of the phosphorus precursor, and therefore amine likely competes with phosphine for coordination to indium.[89] In 2017, Gary et al. studied amine addition to InP clusters and found that amines bound to specific indium centers on clusters, disrupted bridging carboxylate ligands, and upon addition of large amounts (>6 equivalents) of amine, removed up to 4 indium carboxylates from each cluster.[64] Since primary amines alter reaction dynamics so substantially, it is important to consider their role beyond passivation of nanocrystal surface.

1.3.2 Ligand Exchange

Once formed, carboxylate capped InP QDs can be treated with other ligands to modify surface reactivity, particle solubility, quantum yield, or as the first steps of epitaxial shelling. Calvin et al. studied interligand interactions by exchanging oleic acid onto InP QDs synthesized with straight-chain carboxylates of various lengths (myristate, palmitate, and stearate). They found interligand interactions impacted the exchanges, with longer native ligands exchanging more endothermically and slowly than shorter native ligands, and with fully saturated alkyl chains experiencing stronger interactions and more ordered surface packing.[90] When calculating ligand addition energies, Sluydts et al. found that it was favorable for O, F, and all the chalcogens to add superstoichiometrically beyond what the sum-charge rule would predict for InP, with the excess ligands likely adding between bonds, forming bridges, oxidizing, and preventing further epitaxy.[91] This may explain part of the difficulties growing thick, epitaxial zinc chalcogenide-based shells and why InP decomposes in air. Indeed, superstoichiometric L-type binding has been shown to accompany exchanges to carboxylates, thiols, and phosphonates.[67,90,92] (Figure 1.4)

It was theorized that ligand exchanging carboxylates to thiols before ZnS shelling could increase surface passivation and epitaxial growth of the shell since, according to the Hard-Soft Acid-Base (HSAB) theory, the better matched, softer thiol should bind more strongly to indium than the native carboxylate.[92] Unfortunately, the superstoichiometric binding resulted in particle etching and did not significantly improve ZnS shelling epitaxy. This etching can be avoided in situ during ZnS shelling by switching the sulfur precursor source from S-ODE to S-TOP.[93]

Phosphonates, with their higher charge, bind so strongly that there are no direct InP QD syntheses that utilize native phosphonate ligands. Indeed, carboxylate-to-phosphonate exchanges are strongly exothermic, irreversible X-type exchanges that can cause nanocrystal decomposition

before the full exchange.[90,93] It has been speculated that this strong binding could provide a more robust ligand layer but unfortunately, exchanging hexylphosphonic acid onto Cd-oleate capped InP QDs decreased the PLQY and caused core erosion upon exposure to air. [67]

Treating carboxylate-capped InP QDs with metal halides can replace the carboxylate with either the metal halide or cleaved halide (depending of the polarity of the solvent) to passivate either undercoordinated surface phosphorus or indium, respectively. Interestingly, this passivation increases PLQY as indium carboxylates are displaced (with smaller halides producing higher QYs), not with the initial passivation of undercoordinated surface sites. This indicates that the increased electronegativity of the halide ligands may increase fluorescent efficiency by withdrawing negative charge and reducing hole trapping.[94]

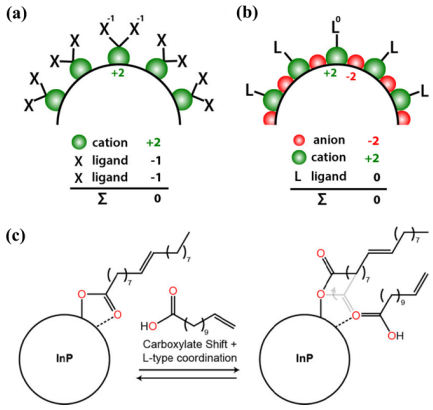

Figure 1.4. (a) Bonding mechanism for X-type ligand binding to surface cations. (b) Bonding mechanism for L-type ligand binding to surface cations. (c) Carboxylate shift from X-type binding to L-type coordination on InP QDs. Reprinted (adapted) with permission from ref. [91] and ref. [92]. Copyright 2019 American Chemical Society.

1.3.3 Surface Oxidation

InP QDs are highly sensitive to oxidation during and after synthesis. This is likely due to the higher covalency of indium phosphide and is readily apparent in the extra degassing and drying steps often seen in InP syntheses. A thick In_2O_3 shell can be grown *in situ* simply by the inclusion of primary amines and carboxylic acids at high temperatures (i.e. 270 °C).[95] In 2010, an NMR study revealed surface phosphides were unintentionally oxidized via the decarboxylative coupling of indium carboxylates that created oxidative conditions *in situ* by producing water as a byproduct.[85] A closer look with X-ray photoelectron spectroscopy (XPS) revealed an amorphous mixed-oxide layer of oxidized indium and phosphorus surface layer on InP QDs and further oxidation during their ZnS shelling likely due to water from ketonization of carboxylic acid formed by Zn carboxylate reacting with H_2S from the side reaction of S with ODE.[96] Since then, InP surface oxidation has been shown to accompany hot injections with indium carboxylates and TMSiP, single-source injections with MSCs formed from indium carboxylates and TMSiP, and shelling steps utilizing Zn carboxylates.[77]

The discovery of this unintentional *in situ* oxidation created a need for a reliable "acid-free" synthesis. Several "acid-free" syntheses report using an indium halide and aminophosphine to avoid water-producing side-reactions and produce oxide-free InP QDs. To avoid oxidation during Zn-based shelling, a Zn halide can be used instead of a Zn carboxylate.[76,77,97] Alternatively, Baquero et al. utilized a novel indium precursor, tris(N,N′-diisopropylacetamidinato) indium(III), with palmitic acid to produce oxide-free InP QDs with carboxylate ligands. This indium amidinate successfully suppressed oxide formation at low temperatures, but at the cost of being unable to grow QDs bigger than 2 nm. Switching to a reducing H_2 environment instead of Ar or N_2 at high temperatures produced oxide-free InP QDs up to 6.7 nm.[45]

Several studies have investigated the effects of water concentration on InP formation and found increasing water concentration produced QDs with narrower, blue-shifted absorbance peaks indicating that water presence might slow precursor conversion rates. The blue-shift also indicates a decrease in particle size, and so it is probable that the water forms a surface oxide that limits growth.[98–100] Furthermore, Kim et al. found that exposing tetrahedral InP QDs to post-synthetic surface oxidation resulted in the loss of faceting during ZnS shelling and the development of an interfacial oxide.[76] Against expectation, Van Avermaet et al. found that once the InP QDs were formed, the addition of surface oxide did not significantly effect emission linewidths or QYs.[101] Other studies have produced InP-based core/shell with higher quantum yields when the InP surface is oxidized, which may indicate that the oxide reduces lattice strain at the core/shell interface.[77,97,99] Others found it more likely that the interfacial oxidation adds interstitially, disrupting the lattice and creating defect-related emission.[102] It may be that both of these are happening concurrently but that the inhomogeneity of an amorphous oxide layer accounts for the differences between these findings.

1.3.4 HF Etching

HF etching is a well-known tactic for increasing InP QD quantum yields that has been used for over 25 years.[103] In initial treatments InP QD syntheses primarily utilized mixtures of TOPO/TOP as passivating ligands and the HF treatments increased QYs from <0.1% up to 40%.[104] It was thought that the HF underwent a photochemical reaction to passivate traps at undercoordinated surface phosphorus atoms and etch away oxidized surface P, allowing increased passivation of newly-surfaced indium with TOPO and fluorine.[104,105]

A recent resurgence of HF etching studies has updated this mechanism for current InP syntheses and proven the reaction of HF with the QD surface to be much more complex than

initially suspected.[73,102,106] It is now thought that fluorine ions bind to surface indium, displacing bulkier carboxylate ligands and relieving steric pressure at the QD surface.[73,106] However, there is still significant debate regarding the mechanism by which fluorination improves PLQY, with arguments supporting the decrease of surface oxidation,[14] removal of electron traps,[73] passivation of hole traps,[94] and even the introduction of shallow hole traps that provide an alternative radiative band-to-trap pathway.[102] By varying the amount of HF used to etch, Kim et al. found that larger quantities photochemically etched InP QDs but smaller quantities underwent a different mechanism, with HF binding to the surface indium without any evidence of etching. Additionally, these smaller quantities of HF caused the absorbance and emission peaks to red shift while the larger etching quantities caused a blue shift. Further complicating this trend, they found that increasing the water content in the smaller HF additions reduced the extent of the HF-induced red shift drastically enough to cause a blue shift.[106] The presence of water as an HF cosolvent provides oxidative conditions that, concomitant with surface fluorination, could photo-oxidize the particle, adding oxygen interstitially. The introduction of oxygen atoms into the lattice would induce internal disorder that could be responsible for the increase in defect-related emission (i.e. emission linewidth broadening toward lower energies) that partially accounts for the increase in PLQY.[102] On the other hand, XPS of InP QDs etched with larger quantities of HF show a reduction in $InPO_x$ binding, indicating the removal of surface oxides.[14] These factors explain the inconsistencies among HF studies in the literature and demonstrate the need for further mechanistic studies.

1.4 Core/shell InP-based QDs

Growing a thick shell of a different semiconductor material around quantum dots provides more robust chemical protection than the labile ligand layer. If the bandgap of the shell material differs significantly from the core nanoparticle, this forms a band structure that controls carrier

localization. Type-I band structures require a shell material with a larger band gap to energetically confine charge carriers to the core and promote exciton recombination. Type-II band structures require a shell material with a smaller band gap to extract charges from the core. Quasi type-II structures have similarly sized band gaps that are offset to confine one charge and delocalize the other charge.

1.4.1 Zn-In Interface

Zn-based shelling (i.e. ZnSe and/or ZnS) is the predominant method of increasing the photoluminescent efficiency and stability of InP QDs. Passivating the surface of InP QDs with Zn carboxylates increases excitonic PLQY and decreases trap PL contribution by passivating undercoordinated surface P and decreasing steric pressure with zinc's lower charge.[73,107] Yet thick, uniform shell growth remains an obstacle. As such, Zn interactions with InP QDs have been extensively studied to elucidate the core/shell interface. Unfortunately, significant variation in synthetic methods has made it difficult to make comparisons and draw consistent conclusions. Foremost among these variations is when during the synthesis the zinc precursors are included: during InP nucleation and growth, immediately after growth (i.e. same pot, without washing), or after washing/purification.

First and foremost, including zinc precursors during InP nucleation and growth can incorporate Zn substitutionally into the InP lattice in addition to binding Zn as a Z-type ligand at the QD surface. There has been significant debate regarding the extent and type of this alloying, especially since the effects from the surface-bound Zn are often difficult to parse from those of the alloying. Nevertheless, Zn alloying has been confirmed with XRD peak shifts toward higher 2θ indicating lattice contraction,[62,87,102] XPS peak shifts indicating changing core bonding environment,[75,108] ICP-OES percent zinc increases indicating increased Zn incorporation even when particle size

remains constant,[75,108,109] and a blue shift of the first excitonic absorbance feature indicating bandgap widening.[75,109,110] It has been noted that the substitutional inclusion of aliovalent Zn into the InP lattice requires either the loss of a negatively charged surface ligand or the creation of a phosphorus vacancy to balance the net charge. DFT calculations have predicted the formation of phosphorus vacancies over the loss of ligands and energy-dispersive X-ray spectroscopy (EDS) measurements have confirmed that, in samples of similar size, the overall %P decreased as %Zn increased.[108] Using statistical parameter estimation theory to extract lattice parameters from high-angle annular dark-field scanning transmission electron microscopy (HAADF-STEM) images of individual alloyed and non-alloyed QDs found that Zn-alloyed InP QDs had contracted lattices with a significantly broader variation in lattice size than the unalloyed QDs. This demonstrated that the extent of Zn alloying was highly inconsistent from dot to dot, and that only a small amount of the Zn present alloyed while the majority was surface bound.[87] Additionally, the extent and type of alloying can change significantly with the synthetic methods used (Figure 1.5), such as varying the ratio of Zn:In precursors,[87,108] including S or Se sources for simultaneous InP growth and shelling,[31,49] varying ligand chain length and purity,[87] and changing the zinc halide size.[60] This heterogenous alloying could vary the bandgap of individual particles causing the broadening of the lowest energy absorbance peak that has been noted in a number of studies.[60,62,87,109] Yet, other studies have found that the inclusion of Zn precursors narrowed the absorbance peak by competing with the indium precursor to form a more stable Zn-P intermediate that slowed growth kinetics and suppressed unwanted nucleation.[33,43,75,110] Further studies are needed to determine the balance between Zn presence reducing morphological heterogeneity by modulating growth kinetics and Zn alloying increasing electronic heterogeneity by varying the bandgap.

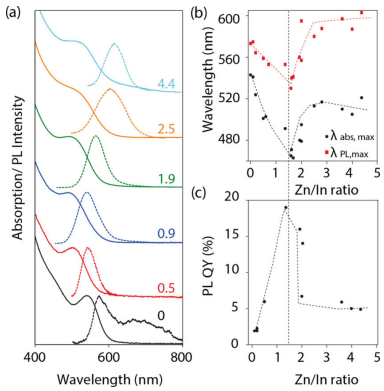

Figure 1.5. (a) Absorbance and fluorescence changes as the ratio of Zn:In is increased during InP synthesis. (b) Absorbance and fluorescence peak max with increasing Zn:In ratio. (c) Change in PL QY with increasing Zn:In ratio. Reprinted (adapted) with permission from ref. [108]. Copyright 2016 American Chemical Society.

1.4.2 Zinc Sulfide Shells

For many years, ZnS was the predominant shelling material since its wide band gap (3.54 eV) ensured strong confinement of both excitonic carriers. Unfortunately, zinc sulfide's large lattice mismatch with indium phosphide (7.8%) has prohibited thick epitaxial shell growth.[31,49,53] It was theorized that an InPZnS alloy, either of the entire particle or just at the interface, could modulate lattice mismatch to reduce strain at the core/shell interface and grow thicker ZnS shells with improved PL properties. For many years, attempts to grow alloyed InPZnS QDs were still unable to produce nanoparticles larger than 5 nm or above 70% QY.[31,53,111] In 2022, Cui et al. found that increasing sulfur content at the core/shell interface reduced lattice mismatch, improved PL QY, and grew InP/ZnS QDs up to 7.5 nm.[63] It is likely that the improved core passivation rather than the increased ZnS shell thickness improved the PLQY since shell thickness studies have shown that PLQY of InP/ZnS QDs is not thickness dependent.[112] Indeed, recent advances in modulating

the InP lattice with zinc alloying have produced thin-shelled In(Zn)P/ZnS QDs with PLQYs up to 92% and emission linewidths as low as 36 nm in blue and green emission wavelengths.[101,113] Unfortunately InP/ZnS QDs emitting at lower energies have not matched this improvement.

1.4.3 Zinc Selenide Shells

Zinc selenide, with its smaller lattice mismatch (3.4%), can grow thick shells (>10 monolayers and >5 nm) but its smaller band gap (2.58 eV) allows excited electrons to delocalize into the shell, causing red shifting with shell growth.[35,93] Comparative studies have found that ZnSe shells generally produce QDs with smaller ensemble PL linewidths, less efficient Auger recombination, longer TRPL decays, and less trapping PL than InP/ZnS QDs yet still have lower QYs.[33,35,60] This may be due to the lower photochemical stability of ZnSe. Selenium has a higher oxophilicity than sulfur and this causes the ZnSe shell to be more susceptible to oxidative degradation.

1.4.4 Complex Zn-based Shells

To take advantage of zinc selenide's smaller lattice mismatch and zinc sulfides photochemical stability, many studies grow a thick ZnSe midshell and then a thin ZnS capping shell. Interestingly, the thickness of the ZnSe midshell does not significantly impact single exciton behavior, but thicker ZnSe midshells experience a slower trapping rate and less efficient Auger recombination of multiexcitons.[114,115] Under high-intensity excitation, two types of biexcitons are likely to form: an 'untrapped' biexciton with two conduction band electrons and two valence band holes and a 'trapped' biexciton or negative trion with two conduction band electrons, one valence band hole, and one trapped hole.[116] The trapped hole has been shown to tunnel, converting the negative trion to the 'untrapped' biexciton, and smaller cores and thinner shells exhibit faster tunneling.[117]

Alloyed ZnSeS shells have been grown on InP QDs by utilizing the difference in S and Se precursor reactivities to confine Se closer to the core. Van Avermaet et al. alloyed sulfur in the

ZnSe midshell to increase the exciton confinement, blue shifting the emission peak. By varying the sulfur content, they successfully tuned the emission color across the visible spectrum (610-490 nm) without altering the InP core size and thus maintained similar emission linewidths across the full spectrum.[101] This alloying can smooth the lattice change from ZnSe to ZnS to reduce lattice strain, but when compared directly, alloyed samples exhibit lower PLQYs than discrete ZnSe/ZnS shelled QDs.[73,108,118,119] In 2019, Lee et al. found that alloyed ZnSeS shells experienced more lattice strain than discrete ZnSe/ZnS shells, causing broader ensemble and single particle PL linewidths.[119] Another study found that this strain was associated with higher sulfur compositions, with lower sulfur composition gradients experiencing reduced strain, better suppressed Auger recombination, and decreased spectral diffusion.[120]

1.4.5 Increasing Fluorescent Efficiency

As synthesized InP QDs display an emission peak attributed to band edge recombination, a broad lower energy peak attributed to deep trap emission and exhibit low PLQYs (<1%) due to extensive carrier trapping at undercoordinated surface sites. These traps are deeper than in II-VI systems due to indium phosphide's higher covalency and they deepen as the size of the QD decreases and the band gap widens.[47] As shown in Figure 1.6, underpassivated surface indium sites act as electron traps, with indium dangling bonds calculated at -3.947 eV, and underpassivated surface phosphorus sites act as hole traps with phosphorus dangling bonds calculated at -5.717 eV.[121–124] Deeply trapped holes can cause InP QDs to remain charged for hundreds of microseconds, quenching PL and favoring Auger recombination.[47]

Surface treatments such as HF etching and Zn or Cd passivation can increase QYs up to 50% (Figure 1.6) by passivating surface electron and hole traps, although the mechanism(s) by which they do are debated.[73,94,108,125] This passivation reduces the trap PL peak, slows early PL decay

dynamics, and increases the Stokes shift, but trapping is not completely eliminated as QYs are only increased to 20-50% and trap emission from band edge electrons to trapped holes broadens or red shifts the main PL peak.[73,102] Density functional theory (DFT) modeling of InP surface trap states predicts that full surface passivation by $InCl_3$ results in no surface trap states, indicating that, at least theoretically, elimination of surface trapping should be achievable.[126] Janke et al. also found that concomitant Raman broadening indicates a link between vibrational properties and emission properties in InP QDs.[102] Hughes et al. pointed out that these surface treatments affect surface cations and thus cannot fully passivate carrier trapping whereas semiconductor shelling can modify both surface cations and anions.[73]

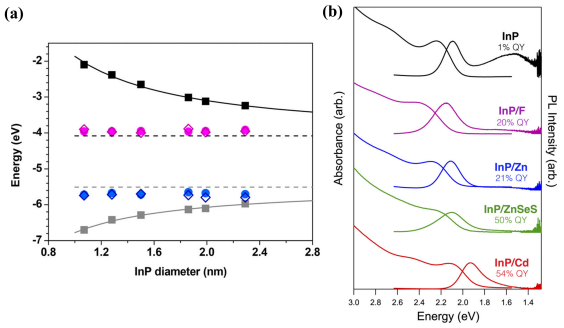

Figure 1.6. (a) Energy of InP QD LUMO (black), HOMO (grey), Indium dangling bonds (purple), and phosphorus dangling bonds (blue), and InP bulk band gap (dashed lines). (b) Absorbance and fluorescence (normalized) of various InP-based QDs with different surface treatments. Reprinted (adapted) with permission from ref. [124] and ref. [73]. Copyright 2019 American Chemical Society.

Shelling InP QDs with ZnSe and ZnS can increase PLQYs up to unity (100%), decrease trapping PL down to 13% of the total PL, and extend biexciton lifetimes by pushing traps closer to the band edges and delocalizing trap orbitals so that they act more like band edge states.[14,33,125]

Recent improvements in controlling the Zn chemistry of ZnSe/ZnS shellings, such as concomitant HF etching, increased shelling temperatures, and entropic ligand mixtures, have produced InP/ZnSe/ZnS QDs with near unity PLQYs and ensemble PL linewidths as narrow as 35 nm.[14,50,75,119] (Figure 1.7) In 2019, Won et al. used HF etching concomitant with the initial ZnSe shell growth to remove oxides from the InP QD surface that impede initial shell deposition.[14] Annealing at high temperature (340 °C) has been shown to promote epitaxial shell growth, producing spherical InP/ZnSe/ZnS QDs rather than lobed or elongated morphologies.[14,41] Li et al. utilized two ligand sources with significantly different chain lengths (termed 'entropic' ligands) during shelling to increase ligand passivation and colloidal stability.[32] Together, these improvements explain the drastic improvement in reported ensemble PLQYs in recent publications. (Figure 1.7c)

Figure 1.7 compares the reported literature values (PLQY, emission peak, linewidth) of the best performing InP-based QDs (>90% PLQY or <40 nm linewidth). Currently, red, blue, and green-emitting QDs have all been produced with >95% PLQYs and <38 nm linewidths but violet, yellow, orange, and near IR-emitting InP-based QDs still need refinement. (Figure 1.7a) Despite most InP syntheses opting to include zinc precursors during InP nucleation, the samples with unalloyed InP cores have produced the most color-pure emission to date. (Figure 1.7b) Recent improvements in controlling aminophosphine chemistry have produced InP-based QDs on par with those utilizing TMSiP. (Figure 1.7c)

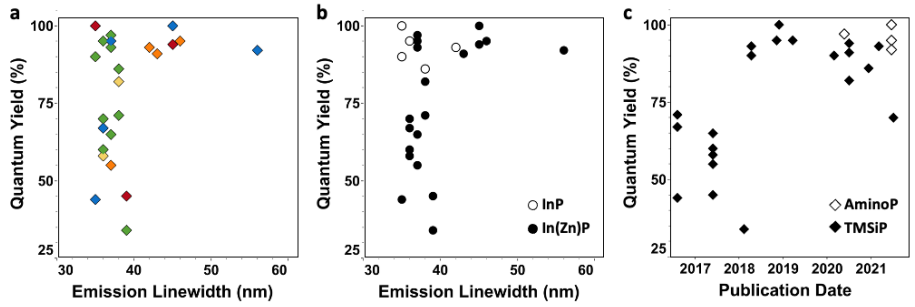

Figure 1.7 Linewidths and PLQYs of the best performing InP-based QDs (<40 nm linewidth or >90% PLQY) from recent publications. (a) Reported linewidths and PLQYs of InP-based QDs with different emission colors (red, orange, yellow, green, or blue). (b) Reported linewidths and PLQYs of InP-based QDs with either alloyed In(Zn)P cores (filled circle) or InP cores (empty circle). (c) Reported PLQYs and publication dates of InP-based QDs synthesized using either TMSiP (filled squares) or an aminophosphine (empty squares). Full data included in Appendix Figure A.1.

Even with these improvements, the ensemble linewidths of InP-based QDs are broader than those of Cd-based QDs. A comparison of commercially available InP-based and CdSe-based QDs found that although the InP sample had a much broader ensemble PL linewidth (178 meV), the single particle linewidths of the InP and CdSe samples were similar (~73 meV).[127] This makes sense considering that InP has a much larger Bohr radius than CdSe causing the band gap of InP QDs to widen faster with decreasing particle size and therefore present a wider ensemble linewidth at similar size distributions.[33] Since then, the single particle linewidths for CdSe-based QDs have been halved (36 meV) by taking advantage of its hexagonal lattice to grow biaxially strained CdSe/CdS QDs while reported single particle linewidths for InP-based QDs have not significantly improved.[7,119] Another factor causing both single particle and ensemble PL broadening for InP-

based QDs is chemical heterogeneity at the core/shell interface. Janke et al. found that the ensemble red PL edge broadening was not due to size-dependent heterogeneity but to trap emission from inconsistent, shallow hole traps introduced by heterogenous Zn lattice substitution at the core/shell interface.[102] The key to further reducing ensemble PL linewidths lies with improving InP QD size distributions and Zn surface chemistry.

1.5 Overview

This work examines the effects of shell composition and morphology on InP QD fluorescent properties. Chapter 2 discusses the experimental methods used in the work to synthesize and characterize InP-based QDs. Chapter 3 examines the impact of indium alloying into the ZnSe shell on the exciton recombination dynamics of InP/ZnSe QDs. STEM-EDS mapping reveals the extent of indium alloying in alloyed and discrete shell InP/ZnSe QDs. Ensemble photoluminescence measurements, including steady state PL, nanosecond lifetime, and femtosecond fluorescent upconversion spectroscopy reveal the photoluminescent efficiency and charge carrier trapping dynamics of these systems. Chapter 4 utilizes a novel STEM analysis method to extract quantitative size and morphological measurements of InP/ZnSe QDs synthesized under a variety of conditions. A methodological study of ZnSe shelling parameters is accomplished by combining ensemble photoluminescence measurements with quantitative size and morphological measurements. Chapter 5 reflects on this work and proposes further experiments for studying InP-based QD systems.

CHAPTER II: METHODS

Commented [CSM3]: CHAPTER II: Methods

2.1 General Air-free Considerations

All glassware was dried in a 120 °C oven overnight prior to use. All reactions, unless otherwise noted, were run under an inert atmosphere of argon using a glovebox or using standard Schlenk techniques. Reactions run on a Schlenk line incorporated a degassing step to remove air and water from chemicals before the synthesis proceeded. Reactions run in nitrogen-filled glovebox were purged with argon and run under an isolated atmosphere. Synthesized quantum dots were purified via centrifugation with solvents stored under sieves either in a centrifuge in the glovebox or in a sealed Teflon centrifuge tube outside the glovebox before storage in the glovebox. It has been shown that carboxylate ligands can participate in side-reactions that produce water *in situ* at high temperatures (>200 C), especially in the presence of TMSiP and/or amines. It is likely that this side-reaction contributes to the *in situ* oxidation of InP QD surfaces during synthesis and shelling and therefore the replacement of carboxylates with halides is recommended to produce oxide-free InP-based QDs.[77]

2.2 Chemicals

Indium (III) acetate (99.99%, trace metals basis), zinc acetate (99.99%, trace metal basis), tris(trimethylsilyl)phosphine (95%), myristic acid (99%), oleic acid (90%, technical grade), 1-octadecene (ODE, 90%, technical grade), oleylamine (OLA, 70%, technical grade), dioctylamine (DOA, 98%) trioctylphosphine (TOP, 97%), acetonitrile (99.8%, anhydrous), and molecular sieves (4A, beads, 8-12 mesh) were obtained from Aldrich. Tri-*n*-octylamine (TOA, 97%) was obtained from Acros Organics. Selenium powder (99.99%, 200 mesh) was obtained from Alfa Aesar. Sulfur powder (99.99%), isopropanol (99.9%), hexanes (99.9%) , and toluene (99.9%) were obtained from Fisher Scientific.

Solvents (octadecene, oleylamine, dioctylamine, acetonitrile, isopropanol, and toluene) were subjected to three cycles of freeze-pump-thaw cycling with liquid nitrogen and high vacuum to remove dissolved gasses before storing in a -filled glovebox over 4 Å molecular sieves.

All other chemicals were used without further purification unless noted otherwise.

2.3 Alloyed and Core/shell InP/ZnSe QDs

2.3.1 Precursor Preparation

Indium myristate ($InMy_3$) was synthesized according to the procedure published by Harris and Bawendi.[58] Briefly, 1.4595 g (5 mmol) indium acetate, 4.1109 g myristic acid, and 50 mL ODE were degassed in a 100 mL three-neck round-bottom flask on a Schlenk line at 120 °C under vacuum for 1 h. The reaction was then placed under an argon atmosphere and heated to 150 °C for 30 min, until the solution became clear. The solution was then further degassed at 110 °C under vacuum for 1 h before being placed back under an argon atmosphere and cooling to room temperature. The white precipitate was vacuum filtered using a M frit funnel and washed with hexanes and deionized water before being transferred to a tared vial, dried under vacuum overnight, and then stored in a desiccator. ^{1}H NMR of precipitate was performed by Alexandra Koziel on a Bruker 400 MHz console equipped with an 9.4 Tesla Oxford magnet with 5 mm Z-gradient broadband (BBFO) probe with automatic tuning and matching capability (ATM). Samples were prepared in deuterated toluene and found full conversion to $InMy_3$ with no acetic acid or water present. (Appendix Figure A.2)

Zinc oleate (0.4 M) was prepared by degassing 2.57 g (14 mmol) of zinc acetate, 9 mL of oleic acid, and 26 mL TOA in a 100 mL three-neck round-bottom flask on a Schlenk line at 120 °C under vacuum for 2 h. The reaction was then placed under an argon atmosphere and heated to 280 °C before further degassing at 120 °C under vacuum for 30 min. The solution was placed back

under an argon atmosphere, cooled to room temperature, and then subjected to three cycles of freeze-pump-thawing to remove dissolved gasses before storing in a nitrogen glovebox.

TOP-Se (0.4 M) was prepared by dissolving 0.95 g (12 mmol) of selenium powder in 30 mL TOP with stirring until completely dissolved in a nitrogen-filled glovebox.

TOP-S (0.4 M) was prepared by heating 0.38 g (12 mmol) of sulfur in 30 mL TOP with stirring until completely dissolved in a nitrogen-filled glovebox.

2.3.2 InP QD Synthesis

InP QD cores were synthesized using a modified literature protocol by Reid et. al.[35] Briefly, 160 mg (0.2 mmol) indium myristate and 5 mL ODE were added to a 100 mL three-neck round-bottom flask in a nitrogen-filled glovebox. The mixture was heated to 150 °C with stirring and argon purging for 30 min. The reaction was then placed under an isolated argon atmosphere and heated to 300 °C. A mixture of 45 μL (0.15 mmol) tris(trimethylsilyl)phosphine (TMSiP) and 1 mL TOP was quickly injected into the reaction flask and the QDs were grown for 30 minutes before cooling to room temperature. The nanocrystals obtained were typically 3 nm in diameter with zinc blende crystal lattice.

2.3.3 Alloyed Shell InPZnSe QD Synthesis

InP QDs were synthesized as described above before 50 mg of zinc myristate and 3 ml TOA were loaded into the reaction flask consisting of freshly made InP cores. The solution was heated to 150 °C with stirring and argon purging for 30 min. The reaction was then placed under an isolated argon atmosphere and heated to 300 °C. A mixture of zinc oleate (3 mL, 0.4 M stock) and TOP-Se (3 mL, 0.4 M stock) was added dropwise into the growth solution at a rate of 1.5 mL/h using a syringe pump for 3 h. The reaction solution was further annealed at 300 °C for 1 h. After cooling to room temperature, the crude InP/ZnSe stock was stored in the glovebox. Samples for

optical and structural characterization were prepared by washing with isopropanol, centrifuging, and re-dispersing in toluene.

2.3.4 Discrete Shell InP/ZnSe QD Synthesis

InP QDs were synthesized as described above. Before shelling, crude InP QDs were washed one time by precipitating with isopropanol, centrifuging, and re-dispersing in toluene. In a 100 mL 3-neck round-bottom-flask, 50 mg of zinc myristate, 5 mL ODE, and 3 ml TOA were heated to 150 °C with stirring and argon purging for 30 min. The reaction was then placed under an isolated argon atmosphere, the washed InP QD stock was injected, and the solution was heated to 300 °C. A mixture of zinc oleate (3 mL, 0.4 M stock) and TOP-Se (3 mL, 0.4 M stock) was added dropwise into the growth solution at a rate of 1.5 mL/h using a syringe pump for 3 h. The reaction solution was further annealed at 300 °C for 1 h. After cooling to room temperature, the crude InP/ZnSe stock was stored in the glovebox. Samples for optical and structural characterization were prepared by washing with isopropanol, centrifuging, and re-dispersing in toluene.

2.4 Methodological Study of InP/ZnSe Shelling Parameters

2.4.1 Precursor Preparation

Indium myristate ($InMy_3$) was synthesized according to the procedure published by Harris and Bawendi.[58] Briefly, 1.4595 g (5 mmol) indium acetate, 4.1109 g (>15 mmol) myristic acid, and 50 mL ODE were degassed in a 100 mL three-neck round-bottom flask on a Schlenk line at 120 °C under vacuum for 1 h. The reaction was then placed under an argon atmosphere and heated to 150 °C for 30 min, until the solution became clear. The solution was then further degassed at 110 °C under vacuum for 1 h before being placed back under an argon atmosphere and cooling to room temperature. The white precipitate was vacuum filtered using a M frit funnel and washed with hexanes and deionized water before being transferred to a tared vial, dried under vacuum

overnight, and then stored in a desiccator. ^{1}H NMR of precipitate was performed by Alexandra Koziel on a Bruker 400 MHz console equipped with an 9.4 Tesla Oxford magnet with 5 mm Z-gradient broadband (BBFO) probe with automatic tuning and matching capability (ATM). Samples were prepared in deuterated toluene and found full conversion to $InMy_3$ with no acetic acid or water present. (Appendix Figure A.2)

$InMy_3TOP_3$ (0.2 M) was prepared by degassing 3.1920 g (4 mmol) $InMy_3$ and 15 mL ODE in a 100 mL three-neck round-bottom flask on a Schlenk line at 120 °C under vacuum for 2 h. The solution was then placed under an argon atmosphere and 5.3 mL (12 mmol) TOP was injected and annealed for 30 min before being cooled to room temperature. The solution was subjected to three cycles of freeze-pump-thawing to remove dissolved gasses before storing in a nitrogen glovebox.

Zinc oleate (0.4 M) was prepared by degassing 2.57 g (14 mmol) of zinc acetate, 9 mL of oleic acid, and 26 mL TOA in a 100 mL three-neck round-bottom flask on a Schlenk line at 120 °C under vacuum for 2 h. The reaction was then placed under an argon atmosphere and heated to 280 °C before further degassing at 120 °C under vacuum for 30 min. The solution was placed back under an argon atmosphere, cooled to room temperature, and then subjected to three cycles of freeze-pump-thawing to remove dissolved gasses before storing in a nitrogen glovebox.

TOP-Se (0.4 M) was prepared by dissolving 0.95 g (12 mmol) of selenium powder in 30 mL TOP with stirring until completely dissolved in a nitrogen-filled glovebox.

TOP-S (0.4 M) was prepared by heating 0.38 g (12 mmol) of sulfur in 30 mL TOP with stirring until completely dissolved in a nitrogen-filled glovebox.

2.4.2 InP QD Synthesis

InP QD cores were synthesized using a modified literature protocol by Xu et. al.[40] Briefly, 1.0 mL (0.2 mmol) $InMy_3TOP_3$ and 4 mL ODE were added to a 50 mL three-neck round-bottom flask

in a nitrogen-filled glovebox. The solution was heated to 150 °C with stirring and argon purging for 30 min. The reaction was then placed under an isolated argon atmosphere and heated to 270 °C. A mixture of 30 μL (0.1 mmol) tris(trimethylsilyl)phosphine (TMSiP) and 1 mL TOP or ODE was quickly injected into the reaction flask and the QDs were grown for 30 minutes before cooling to room temperature. The nanocrystals were purified via centrifugation at 8000 rpm for 10 min with isopropanol and redispersed in toluene. The InP QDs obtained were typically 2.5 nm in diameter with zinc blende crystal lattice.

2.4.3 InP/ZnSe QD Synthesis

InP QDs were synthesized as described above and stored in a nitrogen glovebox. Shell growth was performed using a modified literature procedure by Reid et. al.[35] In a nitrogen glovebox, 6 ml TOA was added into a 100 mL three-neck round-bottom flask. The solution was heated to 150 °C with stirring and argon purging for 30 min. The reaction was then placed under an isolated argon atmosphere and a mixture of 0.1 mmol Zn oleate and 150 nmol InP QDs, concentration calculated according to Achorn et. al. and Talapin et. al., was injected. [70,128] The solution was then heated to 340 °C, and a mixture of zinc oleate (2 mL, 0.4 M stock) and Se-TOP (2 mL, 0.4 M stock) was added dropwise into the growth solution at a rate of 1.5 mL/h for 2 h using a syringe pump. The reaction solution was further annealed at 340 °C for 30 min. After cooling to room temperature, the crude InP-ZnSe core-shell stock was stored in a nitrogen glovebox. Samples for optical and structural characterization were prepared by centrifuging at 10,000 rpm for 10 min with isopropanol and re-dispersing in toluene.

For the methodological study the injection rate was varied from 1 mL/min to 0.025 mL/min, the shelling temperature was varied, in 20 °C increments, from 300 °C to 360 °C, and the trioctylamine was replaced with dioctylamine, oleylamine, or octadecene.

2.5 Characterization

Thorough characterization of QDs was performed to analyze their photophysical properties, size, shape, elemental composition, and crystal structure. Ensemble absorption and emission measurements provide information about QD size, concentration, emission color purity, and fluorescence quantum yield. X-ray diffraction provides information on crystal structure and disorder within the crystal. Time-resolved photoluminescence measurements provides information on fluorescence mechanisms. Single particle spectroscopy reveals photostability of individual QDs. Electron microscopy and energy dispersive x-ray spectroscopy allows for analysis of size, shape, atomic structure, and elemental composition of QDs.

2.5.1 Steady State Optical Absorbance and Emission

All synthesized QDs were initially characterized using static optical absorption and photoluminescence to determine the band gap, nanocrystal size, emission wavelength, color purity (emission FWHM), and fluorescence efficiency. Absorption spectra were recorded on a Varian Cary 60 UV-VIS spectrophotometer. Steady state photoluminescence (PL) spectra were collected on a PTI QuantaMaster fluorescence spectrophotometer using a 75 W Xe arc lamp as the excitation source. PL was measured with a 1 s integration time and a 1 nm slit width.

2.5.2 Photoluminescence Quantum Yield (PLQY)

Photoluminescence quantum yield (PLQY) is a measurement of how efficiently QDs convert absorbed light into emitted photons. Higher PLQY means more efficient radiative recombination of charge carriers. Explicitly, PLQY measures the ratio of photons absorbed by the QD to photons emitted:

$$PLQY = \frac{\#\ photons\ emitted}{\#\ photons\ absorbed}\ x\ 100\%$$

Measurements were taken using the single point calibration method using the laser dye (rhodamine 610 in ethanol, PLQY ~71%). The absorbance of both the QDs and the reference dye were obtained at the excitation wavelength of 500 nm using a Varian Cary 50 UV-Vis spectrophotometer to ensure both had an optical density between 0.09 and 0.1. Their fluorescence was then obtained with a Photon Technology International QuantaMaster 40 and the PLQY was determinced by comparing the integrated emission intensities of the QDs and the reference dye according to IUPAC standards. [129]

$$PLQY = QY_R \frac{I_{QD}}{I_R} \frac{OD_R}{OD_{QD}} \frac{n_{QD}^2}{n_R^2}$$

Where the subscript R is associated with values for the reference dye, the subscript QD is associated with values for the QD sample, I is the integrated fluorescence intensity, OD is the optical density or absorbance of the sample at the excitation wavelength, and n is the refractive index of the solvent used.[130]

2.5.3 InP QD Concentration Calculation

The concentration of QDs in the reaction mixture was calculated according to the procedure by Achorn et. al.[70] by measuring the absorbance of the aliquots at 350 nm to determine the concentration of InP units and by measuring the wavelength of the absorption peak to determine the size of the QDs.

First, the concentration of InP units (c_{InP}, in M) in the reaction mixture was determined by using the Beer-Lambert law with the absorbance of the diluted aliquots at 350 nm (A_{350}), the size-independent molar extinction coefficient of InP units (ε_{350} = 3700 M^{-1} cm^{-1}),[128] the pathlength of the cuvette (ℓ = 1.00 cm), and the dilution factor of the aliquot (D = 101).

$$c_{InP} = \frac{A_{350}}{\varepsilon_{350}\ell} * D$$

Next, the diameter (d, in nm) of the QDs was determined by using the wavelength (λ, in nm) of the absorption peak and the following fit to the data in the dissertation by Talapin:[128]

$$d = 0.02124\lambda - 9.251$$

The number of InP units per QD (N_{InP}) was determined by assuming spherical QDs and using the diameter (d, in nm) of the QDs and the bulk lattice parameter (a = 0.586875 nm) of zincblende InP.[29] The volume of a sphere is $V_{sphere} = \frac{4\pi}{3}\left(\frac{d}{2}\right)^3$, the volume of a unit cell is $V_{cell} = a^3$, and there are 4 InP units per unit cell, so I used the following equation:

$$N_{InP} = \frac{2\pi}{3}\left(\frac{d}{a}\right)^3$$

Finally, the concentration of QDs (c_{QD}, in M) in the reaction mixture was calculated by dividing the concentration of InP units (c_{InP} in M) by the number of InP units per QD (N_{InP}).

$$c_{QD} = \frac{c_{InP}}{N_{InP}}$$

2.5.4 Powder X-ray Diffraction

Powder X-ray diffraction (XRD) analyzes crystal structure of the ensemble QD sample. Powder X-ray diffraction (XRD) measurements were obtained using a Rigaku SmartLab X- Ray diffractometer operating at 40 kV and 44 mA using a Cu Kα line (λ = 1.5418 angstrom) and a D/teX Ultra 250 1D Si strip detector. XRD patterns were collected at a scan rate of 1°/min. Air-free XRD measurements were taken by depositing the sample on an air-sensitive sample holder in a nitrogen-filled glovebox.

2.5.5 Ensemble Time-resolved Photoluminescence (TRPL)

Time-resolved photoluminescence (TRPL) measures the time between absorbance and emission, revealing the lifetimes of the radiative and non-radiative exciton recombination

mechanisms at play. Ensemble TRPL measurements were performed using a custom-built epi-fluorescence microscope.[131] Samples were excited under wide-field illumination using a 405 nm PicoQuant pulsed diode laser with a repetition rate of 2.5 MHz. The beam was reflected with a 420 nm long pass (LP) dichroic filter (Omega Optics, 3RD420LP) into an inverted objective (Olympus UPLSAPO, apochromatic, water immersion, 1.2 N.A., 60x) and brought into focus at the sample. Fluorescence from the focal region was collected by the same objective, passed through the dichroic filter and an additional 450 nm LP dichroic filter, and then focused through a 150 μm aperture onto two single-photon avalanche photodiodes (SPAD, Micro Photon Devices $PD-050-0TC) in a Hanbury-Brown Twiss interferometric configuration. A time-correlated single photon-counting unit (TCSPC, PicoHarp 300, ~35 ps) was used to generate a histogram of photon arrival times. The obtained PL decay curves were fitted using a tri-exponential function with the fit parameters τ_i and A_i are the PL decay time and amplitudes (respectively):

$$I(t) = \sum_{i=1}^{3} A_i e^{\frac{-t}{\tau_i}},$$

The amplitude-weighted average decay time, τ_{avg}, was calculated to approximate the radiative lifetime component, τ_r:

$$\tau_{avg} = \frac{\sum_i^3 A_i \tau_i}{\sum_i^3 A_i}$$

With the ensemble quantum yield, QY, the radiative lifetime component was used to calculate the non- radiative lifetime component, τ_{nr}, such that:

$$QY = \frac{\tau_r}{\tau_r + \tau_{nr}}.$$

2.5.6 Single Particle Spectroscopy

For single nanocrystal blinking measurements, core-shell QDs were diluted to ~ 1 nM concentration in toluene and drop-cast onto a No. 0 glass coverslip. Using the same setup as

described above, samples were excited using a 405 nm PicoQuant electrically pumped laser in wide-field configuration. The beam was focused to a spot ~ 60 μm in diameter with an average excitation power density of ~ 5W/cm^2. Photoluminescence emission from multiple, individual quantum dots was collected through the objective and focused onto an EM-CCD camera (Andor, iXonEM+, DU-897e- CSO-#BV). Intensity-time traces were recorded at 10 Hz (100 ms per frame).

For single nanocrystal spectroscopy measurements, core-shell QDs were diluted to ~ 1 nM concentration in toluene and drop-cast onto a No. 0 glass coverslip. Using the same setup as described above, samples were excited using a 405 nm PicoQuant electrically pumped laser. Photoluminescence emission from individual quantum dots was collected through the objective and focused onto the entrance slit of an Ocean Optics QE spectrometer (600 lines mm^{-1}) equipped with a Hamamatsu, back-illuminated cooled charge-coupled device (CCD) array for detection. Time series of integrated spectra were acquired at room temperature with integration times of 50 ms.

For single nanocrystal lifetime measurements, core-shell QDs were diluted to ~ 1 nM concentration in toluene and drop-cast onto a No. 0 glass coverslip. Using the same setup as described above, samples were excited using a 405 nm PicoQuant pulsed diode laser with a repetition rate of 2.5 MHz. Photoluminescence emission from individual quantum dots was collected through the objective and focused onto two single-photon avalanche photodiodes (SPAD, Micro Photon Devices $PD-050-0TC) in a Hanbury-Brown Twiss interferometric configuration. In this setup, photons emitted from individual QDs were recorded with a series of tags using a time-correlated single-photon-counting (TCSPC, Picoharp 300) unit. All photons were both time-tagged and time-resolved, relative to the beginning of the experiment as well as the

preceding laser pulse in order to simultaneously generate intensity-time traces and PL decay curves.

2.5.7 Transmission Electron Microscopy (TEM), Scanning Transmission Electron Microscopy (STEM), and Energy Dispersive X-ray Spectroscopy (EDS)

TEM allows for analysis of size and shape of the QDs as well as monodispersity. EDS provides information provides information on QD composition through x-rays that are given off by the QDs after their interaction with electrons in the TEM.

Samples were prepared by placing a drop of QDs diluted in hexanes to an optical density of <0.1 onto an ultrathin carbon supported by a Lacey carbon film on a 400-mesh copper TEM grid (Ted Pella, Inc.), wicking away any excess solvent. After QD deposition, the TEM grids were baked under vacuum at 150 °C overnight to remove excess ligands and other organic molecules before imaging.

High-resolution transmission electron microscopy (HR-TEM), scanning transmission electron microscopy (HR-STEM), and scanning transmission electron microscopy with energy dispersive spectroscopy (STEM-EDS) images were taken on a FEI Tecnai Osiris transmission electron microscope operating at 200 keV equipped with a SuperXTM quad EDS detection system. Elemental mapping was analyzed quantitatively using Bruker Espirit 1.9 software. Nanocrystal sizes were determined from STEM images (>500 kx) using the Particle Analysis protocol in the open-source image-processing software Fiji.[132]

CHAPTER III: CONTROLLING CORE/SHELL INTERFACE GRADATION

Commented [CSM4]: CHAPTER III: Shell Alloy

3.1 Introduction

Unpassivated InP QDs are known to show extremely low to no PL emission due to a highly defective QD surface—thought to be dominated by phosphorus dangling bonds.[133] For this reason, InP QDs are typically passivated with a shell of a type-I bandgap material such as ZnS to confine both electrons and holes to the QD core, decoupling them from the QD surface.[37] Unfortunately, the large lattice mismatch between bulk InP and ZnS (7.7%) has limited epitaxial shell growth to a few monolayers. This shell coverage has proven inadequate for full passivation of the InP surface, resulting in QDs with limited PLQYs (~40-60%). Zinc selenide offers a better lattice mismatch (3.4%) while still providing a wide enough band gap to effectively isolate the excitons from the surface. This has produced the first ever thick-shelled (>5 nm) InP/ZnSe QDs, with reduced blinking, narrow PL linewidths, and longer biexciton lifetimes than those seen for InP/ZnS QDs.[34,35]

Recent efforts have investigated more complex shell compositions, such as utilizing multiple shells and alloyed shells.[14,32] For instance, InP/ZnSe/ZnS QDs utilize the closer lattice match of InP-ZnSe to grow an intermediary ZnSe shell that allows for a uniform ZnS shell to be overcoated.[14] This multi-shell approach allows for thick shell growth and increased photochemical stability, but the challenging Zn chemistry has stymied uniform shell growth. Additionally, the complexity of the multi-shell composition makes InP/ZnSe/ZnS QDs a complicated system for studying fine exciton dynamics in InP-based QDs. A simpler shell composition that provides a good option for studying fine exciton dynamics is InP/ZnSe QDs with an alloy at the core/shell interface (hereafter denoted at InPZnSe QDs). Recently, a significant amount of indium incorporation into the ZnSe shell was observed for the first time in InP/ZnSe QDs.[35] Such alloying

of the interface between the CdSe core and CdS shell has been shown to increase the biexciton lifetime and emission efficiency when compared to an abrupt core/shell boundary by relieving lattice strain and relaxing the confinement potential at the interface.[134–136] In fact, alloying of sulfur into CdS_xSe_{1-x} QDs has been shown to completely eliminate hole trapping by decreasing the interactions of charge carriers with the surface of the QD and reducing charge carrier trapping defects at the core/shell interface.[136] But for InP/ZnSe QDs, the valency mismatch between trivalent indium and divalent zinc may also create lattice defects at the core/shell interface that provide in-gap carrier trapping states. The effect of indium alloying at the core/shell interface on exciton recombination dynamics in InP/ZnSe QDs has yet to be studied.

Ultrafast fluorescence upconversion spectroscopy probes charge carrier dynamics on femtosecond timescales and has helped the surface dynamics of QDs to be understood. Extensive work has been performed looking at these carrier dynamics for CdSe QDs.[136–141] For example, the addition of hexadecylamine as a co- solvent while synthesizing CdSe removes the size dependent exciton dynamics and increases the hole trapping time constant.[137] In CdS_xSe_{1-x} QDs, applying a thick shell of CdS with a graded interface to the CdSe core has been shown to completely eliminate hole surface overlap by decreasing the interactions of charge carriers with the surface of the QD and reducing charge carrier trapping defects at the core/shell interface.[136] Some works have studied the ultrafast charge carrier dynamics on InP and InP/ZnS but remains limited as only thin shells of ZnS can be applied to InP cores because the relatively large lattice mismatch between core InP and shell ZnS limits epitaxial growth.[73,142,143]

3.2 InP QD Synthesis and Characterization

InP QDs were synthesized according to the method developed by Reid et. al.[35] where 1 mL of a 0.07 M TMSiP in TOP solution was hot injected into a solution of $InMy_3$ in ODE at 300 °C. This

'original' procedure was carried out on a Schlenk line to avoid InP exposure to oxygen and water because of the susceptibility of InP QDs to oxidation during and after synthesis. Unfortunately, this procedure produced InP QDs with high batch-to-batch size heterogeneity and was also prone to the formation of In_2O_3 nanocrystals-a sign of *in situ* oxygen contamination. In order to reduce in situ oxidation and improve reproducibility, the procedure was modified to perform the synthesis inside a nitrogen-filled glovebox with a faster hot injection. This was accomplished by installing a dedicated Argon gas line in the glovebox for running the synthesis under a contained, pure atmosphere and using a larger gauge needle and syringe for the TMSiP injection. These optimizations resulted in a blue shift of the first excitonic absorption feature (from 561 nm to 542 nm), indicating a smaller nanocrystal size (Figure 3.1 a). Subsequent STEM imaging of the 'original' and 'optimized' InP QDs revealed smaller nanocrystals (3.3 nm vs 3.0 nm diameter) with more uniform shape and decreased size distribution (0.8 nm vs 0.4 nm standard deviation of diameters) (Figure 3.1 c-d). The subpopulation of In_2O_3 nanocrystals, the larger, high-contrast nanocrystals in Figure 3.1 c, was significantly reduced in the optimized synthesis. Additionally, bringing the InP QD synthesis into the glovebox allowed for the introduction of an air-free washing step before storage and shelling.

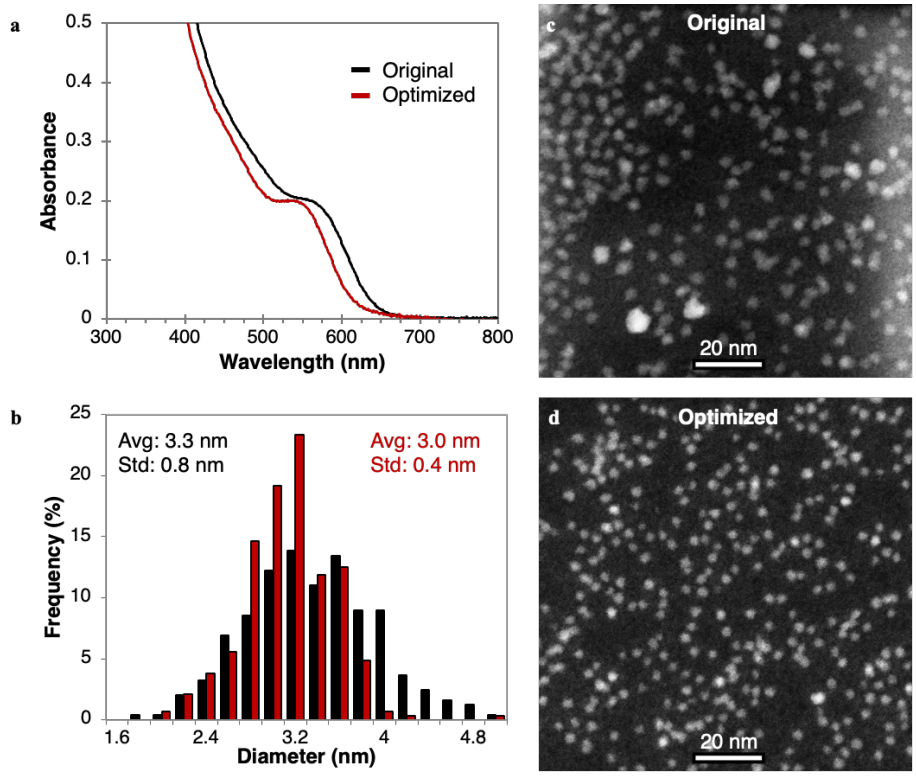

Figure 3.1 (a) First excitonic peak in absorbance spectrum for original synthesis (black) and optimized synthesis (red) InP QDs (b) Histogram of nanocrystal diameters of original and optimized synthesis InP QDs, measured from STEM images by hand (c) and (d) STEM images of original and optimized synthesis InP QDs.

To confirm the crystal lattice of the produced InP QDs, air-free powder XRD and HR-STEM were performed (Figure 3.2). To avoid oxidation during XRD measurement, InP QDs were deposited in the glovebox on an airtight XRD sample holder. The XRD pattern shows the three dominant peaks expected from bulk zinc blende InP. Unfortunately, Scherrer broadening due to the small nanocrystal size masked the less intense peaks. To confirm the zinc blende lattice,

HRSTEM was performed. An FFT (Fast Fourier transformation) of an image of a single, well-aligned InP QD shows a diffraction pattern indicative of a cubic lattice with a d-spacing of 0.33 nm, which matches well with the 0.339 nm d-spacing of bulk InP.[29]

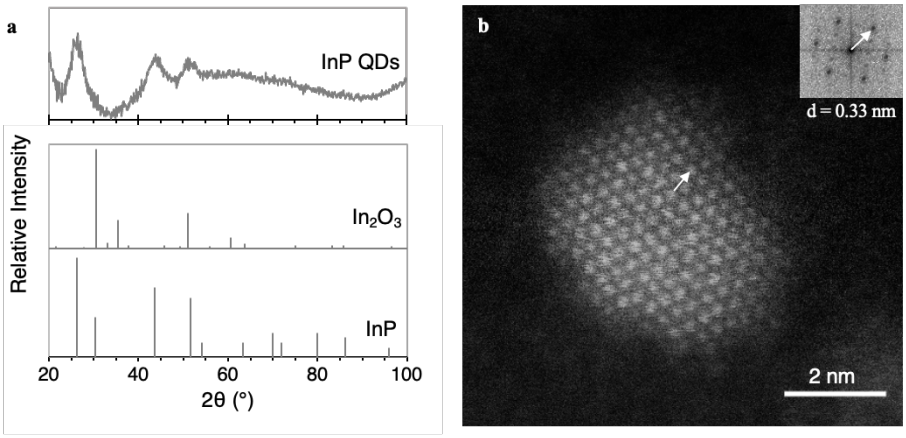

Figure 3.2 (a) Air-free powder XRD of InP QDs, XRD peaks of bulk In_2O_3 , and XRD peaks of bulk InP (b) Background-subtracted HRSTEM and Fourier transformation (inset) of InP QD with the expected 0.33 nm lattice constant of zinc blende crystal lattice.

3.3 Zinc Selenide Shelling of InP QDs

InP QDs were shelled with ZnSe based on a method developed by Reid et. al. utilizing a continuous injection of 0.2 M Zn-oleate and Se-TOP at 300 °C.[35] This publication noted the presence of indium alloyed into the ZnSe shell but did not identify the extent of the alloy or synthetic parameters that led to the alloying. Since then, it has been determined that the presence of excess, unreacted indium precursor during the shelling incorporates indium into the ZnSe lattice.[32,144] Since excess indium precursor is required for the InP QD synthesis, this excess must be removed via a washing step before shelling to minimize alloying.

Two QD samples were prepared using similar InP starting cores, but with a different chemical composition of the shell. QDs with indium incorporated into the shell, referred to as "alloy," were synthesized by following the previously reported procedure of Reid *et al.* where the shelling precursors were injected directly into unpurified cores in their reaction solution.[35] Unreacted indium precursor was thus free to be incorporated into the shell of the nanocrystals and created an interface with both indium and zinc cations between the core and shell of the QDs over the course of the thick shell growth. Conversely, InP/ZnSe QDs with indium restricted to the core, herein referred to as "discrete," were synthesized using a similar procedure with the addition of a purification step after the core InP synthesis that reduced the amount of free indium available during the shelling procedure. As the unreacted indium had been removed, a more chemically abrupt interface was formed between the core and shell of the synthesized QDs.

Figure 3.3 shows the absorbance and photoluminescence spectrum for these two distinct structures. Both QD samples absorb (582 nm alloy/583 nm discrete) and emit (614/612 nm) at very similar wavelengths despite the difference in shell composition. Additionally, both samples show similar PLQY with the alloy QDs at 30% and the discrete QDs at 33%. Hand-drawn diameter measurements of HAADF-STEM images show the discrete shell grew thicker and more evenly than the alloyed shell (9.8 ± 3.7 nm alloy and 11.9 ± 2.7 nm discrete). A closer look with aberration corrected HRSTEM reveals significant defects, with deep divets point defects in both samples. (Figure 3.3 b and d) (aberration-corrected STEM imaging performed by Dr. Matthew Chisholm)

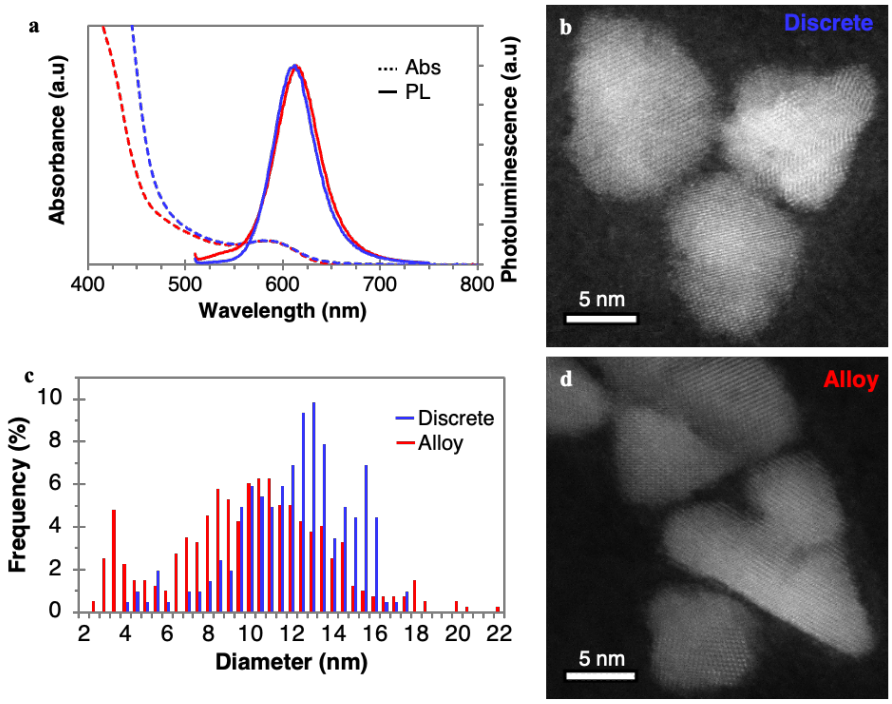

Figure 3.3 (a) Absorbance, photoluminescence, (b,d) HRSTEM images, and (c) size histogram of alloy InPZnSe (red) and discrete InP/ZnSe (blue) QDs. Aberration-corrected STEM imaging performed by Dr. Matthew Chisholm.

Scanning transmission electron microscopy coupled with energy-dispersive x-ray spectroscopy (STEM-EDS) was used to characterize the structure and elemental composition of the synthesized QDs. Similar InP core sizes (3.3 nm) are observed for both the alloy and core/shell samples, which yield the observed absorption and PL. Upon application of a ZnSe shell, the average size for the alloy nanocrystals increased to 9.8 ± 3.7 nm, which is slightly smaller than the discrete average of 11.9 ± 2.7 nm. Toufanian *et al.* have reported little shell-thickness dependence on the photoluminescence lifetimes for Zn-based shelling on InP QDs.[93] With the similar

absorption, emission, and core size between the alloy and discrete QDs, the indium in the shell does not directly contribute to the bandgap of the QDs. Therefore, any measured differences in the ultrafast carrier dynamics can be attributed to the shell composition and not to the slight difference in overall QD size.

Figure 3.4 shows STEM-EDS maps for the two compositions. A difference can be seen where the indium is confined to the core for the discrete QDs, while the alloy QDs show more indium farther from the core. An increase in atomic percentage of indium is seen both for the total QD and the shell of the alloy QDs with atomic percentages of about 3.1% indium and 0.6% phosphorous in the shell. The discrete QDs showed much lower percentages (1.4% indium and 0.3% phosphorous in shell; complete data in the supplementary material). Therefore, while there are trace amounts of indium located throughout both shells, there is significantly more indium consistently alloyed in the alloy sample.

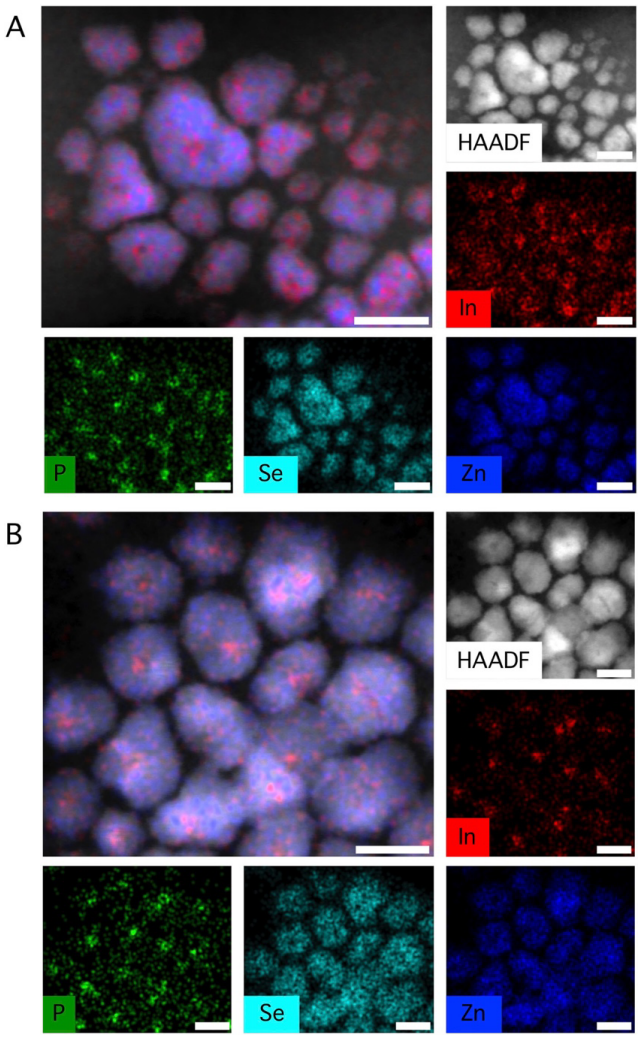

Figure 3.4 High-angle annular dark-field STEM images and EDS maps of indium, phosphorous, selenium, and zinc for (a) alloy QDs and (b) discrete InP/ZnSe QDs. In the alloy QDs, measurable indium extends farther from the core than what is seen for the discrete QDs. Scale bars are 10 nm.

Additionally, aberration-corrected STEM was performed by Dr. Matthew Chisholm at Oakridge National Lab to characterize these thick-shell InP/ZnSe QDs (Figure 3.5). While InP has a lower percentage of lattice mismatch with ZnSe than ZnS, epitaxy of ZnSe onto InP is still challenging. The observed uneven and irregular shell coverage likely contributed to the decreased PLQY observed for both alloy and discrete QDs as it has been shown that defect-free coverage and a reduction in dark QDs are both necessary for high PLQYs.[145] This lack of uniform coverage likely causes structural and electronic defects that negatively affect the optical properties of our InP/ZnSe QDs.[77]

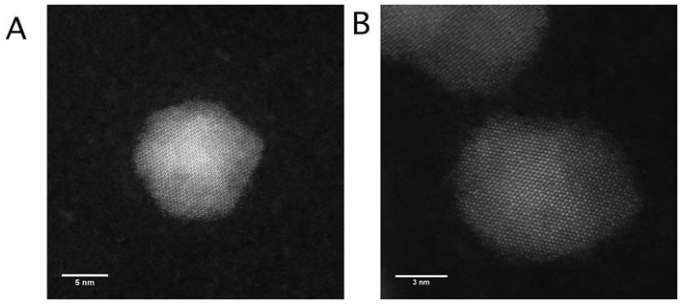

Figure 3.5 (a) Aberration-corrected STEM image of discrete InP/ZnSe QD. (b) Aberration-corrected STEM image of alloy InP/ZnSe QDs. The observed lack of complete shell coverage in some of the nanocrystals is thought to hinder these QDs' PL properties. Imaging performed by Dr. Matthew Chisholm at Oakridge National Laboratory.

3.4 Ensemble Fluorescent Spectroscopy of InP/ZnSe QDs

To investigate the effectiveness of the surface passivation for the two different interfaces, nanosecond lifetimes and femtosecond fluorescence upconversion spectroscopy were used to probe the charge carrier dynamics. Ensemble nanosecond fluorescence lifetimes exhibited similar behavior with average lifetimes of 16.56 ± 0.08 ns for the alloy and 17.92 ± 0.09 ns for the discrete

InP/ZnSe QDs. (Figure 3.6 a) To elucidate the effect of indium alloying on the charge carrier dynamics femtosecond fluorescence upconversion spectroscopy was performed and analyzed by Dr. Nathaniel Freymeyer.[144] This technique allows for preferential probing of the radiative state of a QD system immediately after excitation and without interference from other processes including excited-state absorption and ground-state recovery.[139,146] Nonradiative recombination is therefore observed as a reduction in upconverted fluorescence signal and corresponds to charge carrier localization (trapping). The experiment utilized a femtosecond laser system previously described.[136,138,141] The ultrafast decay curves of both the alloy and discrete InP/ZnSe QDs are plotted in Figure 3.6 b and summarized in Table 3.1.

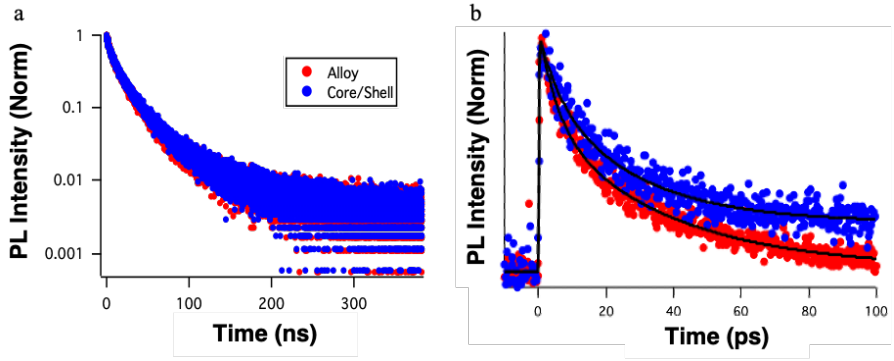

Figure 3.6 (a) Nanosecond fluorescent lifetime for both alloy and discrete InP/ZnSe QDs. (b) Ultrafast fluorescence decay curves (performed by Dr. Nathaniel Freymeyer) for both alloy and discrete InP/ZnSe QDs.

Table 3.1 Ultrafast carrier dynamics for alloy and discrete InP/ZnSe QDs.

	Rel. amp$_2$	**Rel. amp$_3$**	**Rel. amp$_4$**	**τ_1 (ps)**	**τ_2 (ps)**	**τ_3 (ps)**	**τ_4 (ns)**
Discrete	0.22 ± 0.08	0.58 ± 0.08	0.21 ± 0.1	0.1607 ± 0.0124	5.9 ± 2.7	26.1 ± 3.8	17.92 ± 0.09
Alloy	0.38 ± 0.03	0.60 ± 0.02	0.01 ± 0.01	0.1427 ± 0.0087	5.5 ± 0.7	36.8 ± 3.1	16.56 ± 0.08

The rise time (τ_1) has a negative amplitude and reflects the amount of time that it takes for the QDs to begin emitting after excitation and accounts for hot carrier cooling.[136] A very short rise time is observed for both alloy (144 fs) and discrete samples (161 fs) with the alloy sample showing a slightly faster rise time than the discrete sample. These values for InP/ZnSe match closely to previous work on InP/ZnS and InP QDs, which suggests that carrier cooling occurs on very short (~200 fs) timescales and that the rise time is independent of the shell composition.[102] Recent ultrafast transient absorption (TA) experiments on core/alloy/shell InP/ZnSeS QDs again suggest that exciton cooling occurs quickly in InP-based QDs.[147]

Both the discrete and alloy InP/ZnSe QDs exhibit overall fast decays that are attributed to the band alignment between the core InP and shell ZnSe. Given the small offset in the band gap between quantum confined InP and ZnSe, the charge carriers are not fully confined to the core of the QDs and are thus likely trapped both at the interface between the InP and the ZnSe and at the QDs surface. This trapping reduces the amount of radiative recombination that can occur.

A triple exponential decay of both samples was observed, but the decay rate and extent for each process differed. Based upon the effective masses of the charge carriers for InP (m_h = 0.65, m_e = 0.067), the decay components are assigned to hole trapping (τ_2), electron tapping (τ_3), and

radiative recombination (τ_4).[136] The long-lived radiative recombination component of the decay, τ_4 , extends past the lifetime of this ultrafast fluorescence upconversion experiment and was measured with the nanosecond experiment. Figure 3.7 summarizes the differences in carrier dynamics between the two samples based on the relative amplitudes of each decay constant.

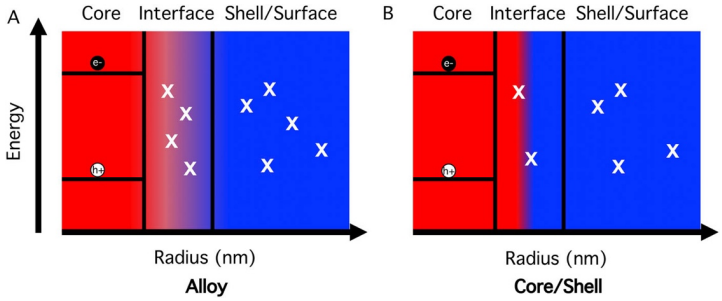

Figure 3.7 Summary of charge carrier dynamics in thick-shell InP/ZnSe QDs by Dr. Nathaniel Freymeyer. More extensive trapping occurs in the alloy QDs than in the discrete QDs. The incorporation of indium into the shell allows for rapid localization of charge carriers at many interfacial sites.

The second decay constant, τ_2, and its relative amplitude reveal that rapid hole trapping contributes a smaller overall portion to the observed decay for both samples compared to τ_3, which is associated with electron trapping. The domination of electron trapping matches previous work carried out by Rowland *et al.* who observed electron trapping as the dominant trapping mechanism in InP and InP/ZnS QDs by ultrafast TA spectroscopy.[148]

While both systems show similar trapping time constants, the extent of trapping for the alloyed QDs is greater than what is seen for the discrete QDs, particularly for rapid hole trapping. Since the electron microscopy indicates that both alloy and discrete particles exhibit similar morphologies, the only major difference would be the inclusion of a higher amount of indium in

the shell. This finding indicates that the inclusion of In^{3+} creates a vehicle for accelerated hole trapping. In and P have been shown to be electronic dopants for II–VI semiconductors and generate intra-gap states serving as non-radiative recombination centers.[32] For the case where indium atoms are incorporated into ZnSe, two additional energy levels are generated 0.59 eV and 0.41 eV above the valence band, which provide multiple states for extensive trapping.[149] These additional energy levels allow for rapid localization of the charge carriers and prevent radiative recombination. The more extensive trapping in alloyed QDs confirms that indium alloying is detrimental to long-lived carriers and thus their radiative recombination.

Although the chemical composition of the thick ZnSe shell is different between these QD systems, the overall ultrafast carrier dynamics remain similar. This similarity indicates that the structural irregularities in the shell coverage revealed by the aberration-corrected STEM images in Figure 3.5 are more influential than the indium dopant states. These states rapidly populate and then remain saturated, resulting in similar static quantum yields as the discrete samples. However, the defect states created by the indium in the shell will likely limit the maximum attainable quantum yield through improved shell passivation. An additional layer of a material with higher energy of the conduction band should enhance the PLQY by preventing the electron from reaching the surface trap states.[150] ZnS provides a wider bandgap and should better confine charge carriers but comes with greater lattice mismatch and greater defects at the interface between the core and shell, which can also prevent charge carrier recombination. Therefore, minimizing the extent of indium alloying and growing an outer layer of a wider bandgap material (ZnS on top of the ZnSe layer) are both important next steps in the development of an ideal InP QD system. Won *et al.* and Lee *et al.* have made significant progress recently on improving the brightness and structure of InP/ZnSe/ZnS QDs.[14,119]

3.5 Conclusions

Discrete and alloy thick-shell InP/ZnSe QDs were synthesized by varying the amount of indium incorporated into the ZnSe shell. These QDs were characterized with extensive structural and optical data to investigate the effect on charge carrier dynamics. While both QD systems offer a thick-shell architecture, which should help increase radiative recombination in QDs, ultrafast fluorescence upconversion spectroscopy data revealed that extensive charge carrier localization still occurs in both QD structures. Extensive carrier trapping in the alloyed QDs suggests that minimizing alloying is required when applying a II–VI semiconductor shell to a III–V core.

CHAPTER IV: QUANTITATIVE STEM ANALYSIS OF ZINC SELENIDE SHELL MORPHOLOGY

Commented [CSM5]: CHAPTER IV: STEM Analysis

4.1 Introduction

Quantum dots (QDs) are semiconductor nanocrystals whose tunable electronic properties make them useful as photon emitters and charge separators in a wide array of applications including solid state lighting,[10,11,14] lasing,[7–9] bioimaging,[6,151,152] 3D printing,[153] luminescent solar concentrators,[154] photovoltaics,[155] and photonic quantum technology.[15,156] QDs have a unique structure-function connection that arises from the quantum confinement of their electrons and causes their electronic properties to become dependent on the nanocrystal structure.[1] This dependence is clearly illustrated by the increasing photoluminescent (PL) energy with decreasing QD size.[4] This structure-function dependence causes QD size, morphology, crystallinity, and surface binding to dictate their electronic properties.[4,136,157–159]

Nanocrystal size can be revealed with dynamic light scattering (DLS),[160] atomic force microscopy (AFM),[161] powder X-ray diffraction (XRD),[162] and transmission election microscopy (TEM).[163] The most accurate of these methods is TEM, which can resolve nanocrystal lattice fringes but is limited by electron diffraction contrast convoluting nanocrystal contrast. Scanning transmission electron microscopy (STEM) minimizes diffraction contrast by collecting only highly scattered electrons. Using an annular electron detector to perform high angle annular dark field (HAADF) imaging provides atomic-number or Z-contrast that can resolve nanocrystal structure down to columns of individual atoms.[164] Despite the high spatial resolution in STEM and TEM images, analysis methods for extracting nanocrystal size and morphology from STEM and TEM images are either too simplistic, limiting the precision and accuracy of size measurements, or are

reliant on computationally demanding approaches that require high quality samples with specific geometries.[40,46,165–168]

The simplest methods are limited to rudimentary sizing measurements estimated by hand-drawn particle diameters. These methods are time-consuming and rely only on qualitative descriptions of morphology set by the individual carrying out the analysis, thus compounding variation with each subsequent analysis. Recently developed automated methods have the advantage of fast, reproducible, high-throughput analysis of both nanoparticle size and morphology but require high quality, uniform samples.[168] Therefore, there is a need to implement an analysis method that can precisely extract size and morphology measurements from electron microscopy images of a wide variety of nanoparticle samples. The open-source image processing software Fiji (Fiji is Just ImageJ) contains a Particle Analysis feature that can be easily adapted to reproducibly extract accurate and precise size and morphological measurements from STEM images of nanoparticles.[132]

Indium phosphide-based QDs offer a cadmium-free QD alternative whose emission can be tuned throughout the visible spectrum.[88] Recent shifts from ZnS to ZnSe/ZnS shells have produced bright, color-pure samples and opened the floodgates for successful synthetic studies.[14] But the difficult zinc chemistry often results in uneven shell morphology that is difficult to correlate with PL behavior due to imprecise size and morphological measurements. Precise morphological analysis is needed to elucidate the role of different synthetic conditions on the zinc chemistry to grow thick, uniform Zn-based shells. Here, we present a methodological study combining quantitative morphological analysis of STEM images in Fiji Particle Analysis with trends in ensemble fluorescence of InP/ZnSe QDs to differentiate the impact of key shelling parameters in InP core passivation and ZnSe shell morphology.

4.2 Fiji Particle Analysis vs. Hand Analysis

There is a plethora of methods for extracting nanoparticle size and morphology information from electron microscopy images. The simplest procedures employ hand-drawn cross-sections to approximate nanoparticle diameters.[40,46] These procedures are useful because they can easily be applied to almost any sample material, morphology, or heterogeneity but their simplicity is also their limiting factor. Hand-made length measurements assume particle geometry (i.e. diameter assumes circular or spherical shape), require qualitative visual assessment to discern morphological trends, and their reliance on human measurements introduces significant error. A recent push to develop precise, high-throughput measurements has produced numerous machine learning and segmentation-based methods to analyze nanoparticle size and shape.[165–168] Unfortunately, these methods rely on shape classification systems that require relatively uniform, geometrically shaped samples. The computational complexity of these methods better suits them to high throughput analysis of well-characterized nanoparticles for quality assessment rather than to morphological characterization of novel nanoparticles produced in a research setting. The Particle Analysis feature in open-source software Fiji combines the precision and reliability of automated procedures with the simplicity and versatility of hand measurements.

To demonstrate the precision and reliability of the Fiji Particle Analysis method, hand measurements taken by three researchers were compared with Fiji Particle Analysis measurements of InP/ZnSe QDs with a lobed shell morphology. InP/ZnSe QDs were synthesized based on a modification of the method developed by Reid *et al*.,[35] utilizing a continuous injection shelling method at 340 °C to grow a thick ZnSe shell on an InP core (~2.4 nm diameter) to produce QDs with a single PL peak centered at 623 nm, a full width at half max (FWHM) of 56 nm, and a photoluminescence quantum yield (PLQY) of 48% (Figure 4.1 A).

For the Fiji Particle Analysis method, particle perimeters of InP/ZnSe QDs were extracted from STEM images using contrast-based manual thresholding and then measured as a function of particle area (nm^2) and Feret diameter (a.k.a. caliper diameter, the longest length between two parallel lines tangential to a particle's silhouette). Lower thresholds were used for the smallest nanoparticles (area <25 nm^2) since their smaller volumes produce lower contrast in HAADF-STEM. All images were subjected to a Gaussian filter of 2 pixels before thresholding to reduce noise. All images analyzed were taken at the same magnification, 630 kx, to maximize analysis resolution. Particle diameters from these same images were independently hand measured by three researchers so that each analyzed particle had 3 hand-measured diameters, 1 Feret diameter (i.e. maximum caliper), and 1 particle area. (Figure 4.1 B) The results of these measurements are summarized in Table 4.1.

At 14.76 nm, the average Feret diameter is 0.7 nm longer than the average hand diameter. (Figure 4.1 C) Additionally, the hand diameters for each particle vary an average of 0.8 nm, with measurements on the same particle varying up to 3.7 nm. The lack of precision with hand measurements introduces a significant source of error into the measurement. Combined with the inherent error from using a one-dimensional measurement to describe the size of a three-dimensional particle, the human-basis of hand-measured diameters significantly limits the precision of the diameter size measurement. Fiji's Particle Analysis method offers another size measurement, particle area (nm^2), that more accurately reflects the sample size than diameter by approximating the 3D size of particles with a 2D measurement rather than the 1D diameters. Measuring the particle areas reveals an average particle area of 123.85 nm^2 with a mean standard error of 1.58 nm^2 or 1.28% and a standard deviation of 26.77 nm^2 or 21.62%. The standard deviation in the area measurement is significantly larger than the standard deviation of the hand

diameters and the Feret diameter, which more accurately reflects the uneven shelling that is masked by a single dimensional measurement.

Table 4.1 Results summarizing particle analysis measurements (Feret diameter) and hand measurements (Diameters 1, 2, 3, and Avg) of InP/ZnSe QDs (n=286).

	Diameter 1	Diameter 2	Diameter 3	Diameter Avg	Feret
Analysis time (min)	55	100	98	84	30
Average (nm)	13.8	14.2	14.1	14.1	14.76
Min (nm)	5.1	5.1	5.1	5.1	5.17
Max (nm)	18.8	18.8	19.3	18.7	19.33
Standard Deviation (%)	14.1%	13.8%	13.7%	13.5%	13.6%
Standard Error (nm)	0.1	0.1	0.1	0.1	0.12

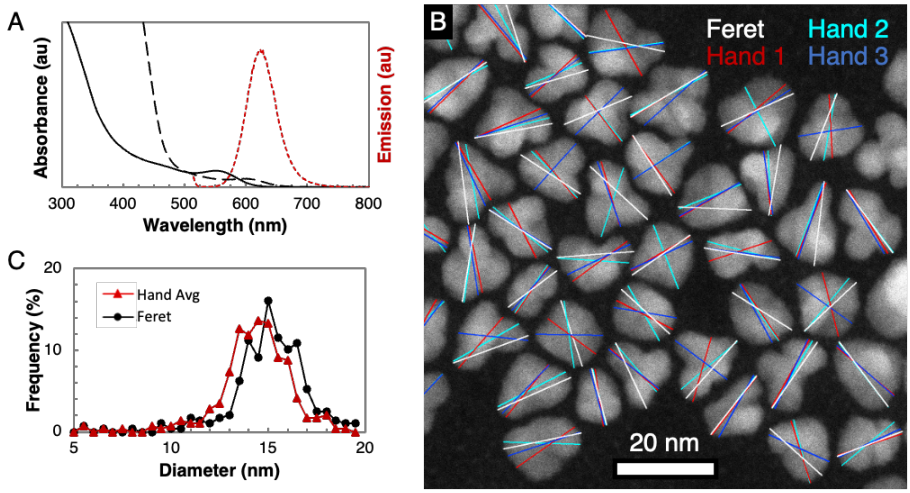

Figure 4.1 (A) Absorbance of InP QDs (black), InP/ZnSe QDs (black dashed), and PL of InP/ZnSe QDs (red dashed). (B) STEM image of InP/ZnSe QDs with overlays of hand-drawn diameters (cyan, red, and blue) and Feret diameters (white). Scale bar is 20 nm. (C) Histogram of InP/ZnSe QD hand-drawn diameters (red) and Feret diameters (black).

4.3 Quantitative Morphological Analysis: Shelling Rate

Nanoparticle morphology, in addition to size, is important for photonics, plasmonics, catalysis, and nanomedicine.[159,169–171] Morphology affects these functions by dictating surface area, surface binding, and nanoparticle anisotropy. In core/shell QDs, surface defects, stacking faults, surface roughness, divots, and uneven shell epitaxy have all been shown to reduce PL efficiency by promoting nonradiative exciton recombination pathways.[157,159,172] Despite this clear structure-function correlation, morphological assessments are almost always qualitative visual assessments of electron microscopy images. These qualitative assessments are limited to sweeping generalizations of visually discernable differences or pinpointing specific lattice defects on individual nanoparticles. There is a need for quantitative metrics of nanoparticle morphology to assess global morphological trends. In addition to size measurements, the Fiji Particle Analysis method measures morphological parameters (circularity, roundness, and solidity) that quantitatively describe particle morphology. Of these parameters, solidity offers a quantitative metric to assess variation in shell thickness across a nanoparticle by comparing the area of the particle with the area of its convex hull area. (Figure 4.2)

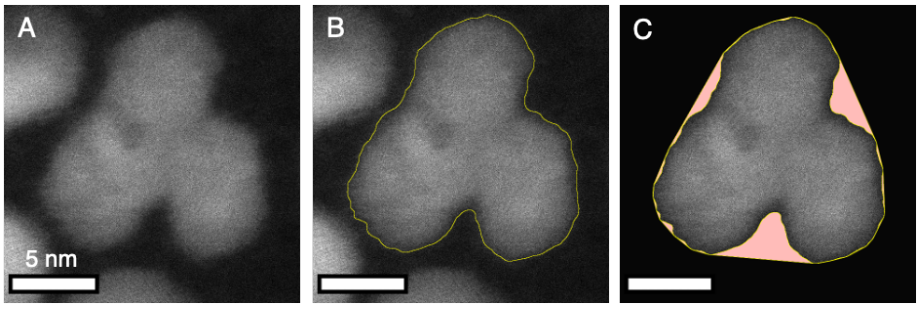

Figure 4.2. (A-C) STEM images of a InP/ZnSe QD. (B) STEM image of same InP/ZnSe QD with particle perimeter overlayed. (C) STEM image of same InP/ZnSe QD with convex hull overlayed.

The solidity of the QD is calculated as a ratio between the area within the particle perimeter and the area of the convex hull.

To test the ability of solidity to discern particle morphology, we varied the ZnSe shelling injection rate from 1 mL/min to 0.025 mL/min. With decreasing shelling rate, the emission peak red shifted slightly (from 619 nm to 626 nm) and narrowed (from 61 nm to 53 nm FWHM). The PLQY increased with decreasing rate until it peaked at 48% with 0.05 mL/h and dropped to 39% with 0.025 mL/min. Qualitative analysis of STEM images of the samples reveals a general trend of increasing size and more even morphology as the shelling rate was decreased but all samples display particles with divets and lobed shell growth that are difficult to differentiate between shell rates. (Figure 4.3A-D) Fiji Particle Analysis on these same images finds that the average particle area increased from 101.57 nm^2 to 135.92 nm^2 with decreasing shelling rate. (Table 4.2) Despite the samples having qualitatively similar morphologies, all four samples have statistically different solidity distributions, with $p < 0.01$ according to both the Kolmogorov-Smirnov test and Mann-Whitney test. Matching the PLQY trend, the InP/ZnSe QDs shelled at 0.05 mL/min have the highest average solidity and the smallest size distribution, indicating a more even shelling morphology that would otherwise be indiscernible. A closer look at the distribution of solidities reveals a subpopulation of lower solidity particles that shifts toward higher solidities with decreasing shelling rate until 0.05 mL/min. (Figure 4.3E) Furthermore, analysis of the size distributions does not reveal this same trend, (Figure 4.3F) indicating the need for morphological measurements in addition to size measurements to fully assess nanoparticles.

Table 4.2. Results of Fiji Particle Analysis of InP/ZnSe QDs with varied shelling rates.

Rate (mL/min)	**1 (n=541)**	**0.1 (n=454)**	**0.05 (n=545)**	**0.025 (n=827)**
PLQY (%)	35%	44%	48%	39%
Emission Peak (nm)	619	623	623	626

Emission FWHM (nm)	61	58	56	53
Area (nm^2)	101.57	110.18	126.75	135.92
Area Stdr. Error	0.98	1.15	1.11	1.15
Solidity (%)	91.852%	92.804%	94.048%	93.672%
Solidity Stdr. Error	0.156%	0.148%	0.111%	0.091%

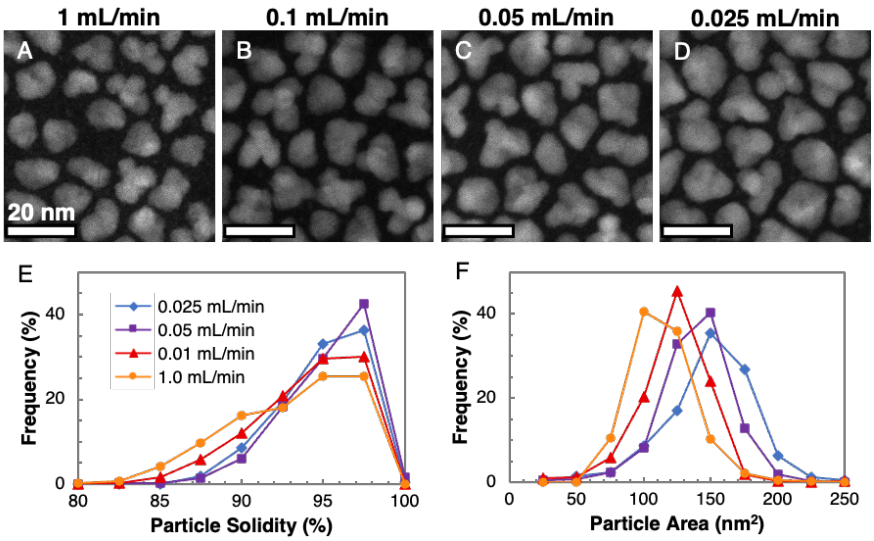

Figure 4.3. (A-D) STEM images of InP/ZnSe QDs shelled with varied injection rates. (E) Frequency diagrams of solidities of InP/ZnSe QDs shelled with varied injection rates. (F) Frequency diagrams of sizes of InP/ZnSe QDs shelled with varied injection rates. Particle areas and solidities of all four samples have statistically different distributions, with $p < 0.01$ according to the Kolmogorov-Smirnov test.

4.4 Quantitative Morphological Analysis: Shelling Temperature

Next, we investigated the role of shelling temperature on shell morphology. It has been shown that increasing Zn shelling temperatures from 300 °C to 340 °C produces InP/ZnSe/ZnS QDs with more even shell coverage and higher PLQY.[14,41] A quantitative morphological analysis of this trend can further dissect the roll of shell coverage to differentiate between shell morphology and core passivation. Ensemble fluorescent measurements indicate how changes to the core surface during initial monolayers of shell growth effect core passivation. By comparing trends in fluorescence properties with morphological changes, we can evaluate how shelling conditions effect core surface chemistry and epitaxial shell growth.

InP/ZnSe QDs were shelled at 320 °C, 340 °C, and 360 °C to assess how the increased shelling temperature affects shell growth. The results are summarized in Table 4.3. Increasing the shelling temperature from 320 °C to 360 °C red shifts the ensemble emission peak from 600 nm to 624 nm while also broadening the emission peak from 43 nm to 47 nm FWHM. The reduced confinement due to the ZnSe band gap is expected to cause red shifting with the first few monolayers of ZnSe deposition but since these sample all have thick shells (>5 nm), this indicates a change in core size.[93] Fiji Particle Analysis on STEM images of these samples reveals increasing particle size from 106.64 nm^2 to 141.43 nm^2 with increasing shelling temperature from 320 °C to 360 °C. (Figure 4.4A-C) The increased temperature likely causes *in situ* defocusing and ripening of the InP core. The PLQY increases slightly from 41% to 47% with the temperature increase from 320 °C to 340 °C and then drops significantly to 23% during the 360 °C shelling. This drop in PLQY signifies a change in core passivation which may be due to ligand decomposition from the high temperature.

Shelling at higher temperatures (340 °C and 360 °C) significantly increases the average particle solidity but the distribution of sizes and solidities for the 360 °C shelling are significantly broader than for the 340 °C shelling. (Figure 4.4D-E) The increase in size distribution paired with the high solidity and the 360 °C shelling indicates that the better control of the Zn chemistry afforded at higher temperatures is being countered by less effective core passivation that reduces PLQY.

Table 4.3 Results of Fiji Particle Analysis of InP/ZnSe QDs synthesized with varying shelling temperatures.

Temperature (°C)	**320 °C (n=660)**	**340 °C (n=579)**	**360 °C (n=441)**
PLQY (%)	41%	47%	23%
Emission Peak (nm)	600	610	624
Emission FWHM (nm)	43	45	47
Area (nm^2)	106.64	137.89	141.43
Area Stdr Error (nm^2)	1.40	1.46	3.11
Solidity (%)	93.859%	95.585%	95.263%
Solidity Stdr Error (%)	0.097	0.067	0.119

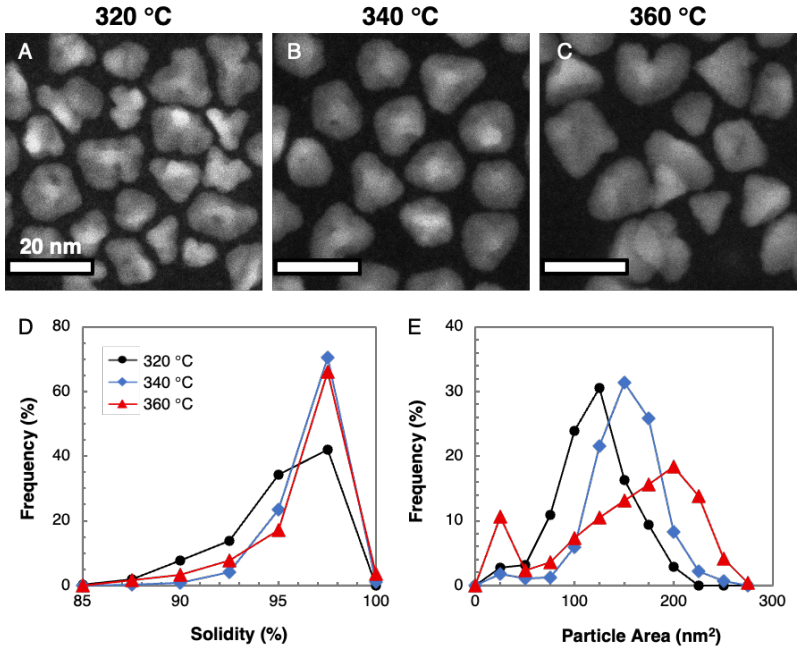

Figure 4.4. (A-C) STEM images of InP/ZnSe QDs shelled at varied temperatures. (D) Frequency diagram of solidities of InP/ZnSe QDs shelled at varied temperatures. (E) Frequency diagram of sizes of InP/ZnSe QDs shelled at varied temperatures. Particle areas and solidities of all three samples have statistically different distributions, with $p < 0.01$ according to the Kolmogorov-Smirnov test.

4.5 Quantitative Morphological Analysis: Ligand Effects

Trioctylamine (TOA) is commonly used as both surfactant and solvent for high temperature shellings (>300 °C) due to its high boiling point, ease of use, and purported shape control at 340 °C.[14] To test the role of amine sterics on particle shape control, TOA was exchanged for several other amines including a secondary amine (DOA), a primary amine (OLA), and a non-coordinating

amine (ODE). Long-chain amines were chosen for their high boiling points, but the annealing temperatures still had to be reduced to 300 °C to accommodate the lower boiling point of dioctylamine (~298 °C). Increasing the steric bulk of the amine from primary to secondary to tertiary maintained the PLQY and emission peak energy of the InP/ZnSe QDs but decreased the emission energy line width. Fiji Particle Analysis, summarized in Table 4.4, reveals that dioctylamine produced the thickest shells with the smallest size distribution and most even morphology, oleylamine produced the thinnest shells with the most uneven morphology, and trioctylamine broadened the size distribution despite suppressing emission line widths. (Figure 4.5A-F) Increasing the shelling temperature to 340 °C with trioctylamine improves the size distribution and shell morphology similar to using dioctylamine at 300 °C. (Appendix Figure A.3) Replacing the amine with non-coordinating octadecene resulted in the lowest line width but the largest size distribution. While these findings initially seem at odds, they highlight how synthetic conditions during shelling affect both the core QD and the epitaxial shell growth. In this case, the basicity of the amines likely causes etching of the InP cores during heat up and initial shell growth, causing increased ensemble heterogeneity via Ostwald-like ripening that increases the ensemble line widths. Once a thin ZnSe layer is deposited, the amines interact with the shell material, acting as ligands to facilitate further shell growth and final shell morphology. Although the etched cores display broader linewidths, the etching may also remove oxidized surface atoms, creating a more even surface for more uniform shell growth that reduces the final size distribution of the InP/ZnSe QDs.

Table 4.4. Results of Fiji Particle Analysis of InP/ZnSe QDs synthesized with varied amines

	OLA (n=219)	**DOA (n=285)**	**TOA (n=216)**	**No Amine (n=295)**
PLQY (%)	25%	25%	25%	21%

Emission Peak (nm)	625	624	624	625
Emission FWHM (nm)	81	70	62	61
Area (nm^2)	90.6	132.3	116.9	123.0
Area Stdr. Error (nm^2)	1.9	2.1	2.9	2.9
Solidity (%)	93.85%	95.65%	94.90%	95.27%
Solidity Stdr Error (%)	0.19	0.11	0.13	0.13

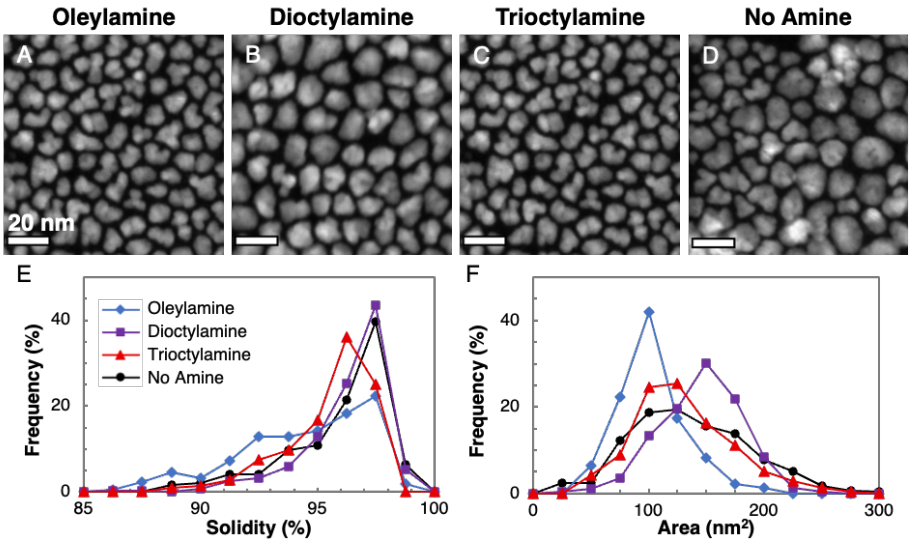

Figure 4.5. (A-D) STEM images of InP/ZnSe QDs shelled with varied injection rates. (E) Frequency diagram of solidities of InP/ZnSe QDs shelled with varied injection rates. (F) Frequency diagram of sizes of InP/ZnSe QDs shelled with varied injection rates. Particle areas and solidities of all four samples have statistically different distributions, with $p << 0.001$ according to the Kolmogorov-Smirnov test, except for the solidities of DOA and No amine ($p < 0.1$) and the areas of TOA and No amine ($p < 0.5$).

4.6 Conclusions

Herein, quantitative morphological measurements were used to discern variations in InP/ZnSe QDs and elucidate the effects of synthetic parameters on shell growth. Using the semi-automated Particle Analysis protocol in the open-source image processing software Fiji to extract particle perimeters from STEM images provides more precise size measurements than traditional hand-drawn diameter measurements by removing the reliance on human measurements. Furthermore, measuring nanoparticle size as a function of two-dimensional area more accurately reflects sample heterogeneity that is masked by the one-dimensional diameter measurement. The Particle Analysis protocol also provides quantitative morphological parameters that can reproducibly find morphological variations that qualitative analysis cannot discern. Combined, quantitative morphological analysis with fluorescence measurements discern how changes in synthetic shelling conditions can deleteriously etch the unprotected InP core yet simultaneously increase even shell epitaxy.

CHAPTER V: CONCLUSIONS AND FUTURE DIRECTIONS

Commented [CSM6]: CHAPTER V: Conclusions

5.1 Overall Conclusions

The first thick-shelled InP-based QDs were first synthesized by Dr. Kemar Reid in 2018 via continuous injection of Zn and Se precursors on InP cores at high temperature.[35] These thick shells were realized by switching from the traditional shelling material, zinc sulfide to zinc selenide, a material with better lattice size match with InP. This accomplishment opened the door to the creation of bright, photostable InP-based QDs for implementation in solid state lighting applications. Since then, red, blue, and green-emitting InP/ZnSe/ZnS QDs with >95% PLQYs and <38 nm linewidths have been successfully produced.

While Dr. Reid was the first to grow thick, epitaxial ZnSe shells on InP QDs, I was able to further optimize the InP QD synthesis and shelling procedure to reduce unwanted InP oxidation and control the shell morphology and composition. During these optimizations, I discovered that the presence of excess indium precursor during the ZnSe shelling led to the alloying of indium into the ZnSe shell. By introducing an air-free washing step before shelling, I was able to minimize this alloying a form a more discrete core/shell structure. Interestingly, this alloying did not cause significant changes to the ensemble steady-state or nanosecond photoluminescence. Ultrafast fluorescence upconversion spectroscopy performed and analyzed by Dr. Nathaniel Freymeyer revealed that the alloyed indium created in gap states for hole trapping.[144] However, the dominant trapping dynamic was electron trapping in the ZnSe shell of both compositions. These experiments were the first in-depth study of the effects of core/shell interface composition on InP QD carrier trapping dynamics.

These results made it clear that the uneven ZnSe shell morphology was limiting PLQY by causing significant electron trapping. To optimize the ZnSe shelling and improve PLQY, a method

for quantifying shell morphology was needed. The open-source image processing software, Fiji offers a Particle Analysis tool that was originally created for the analysis of biological particles. I adapted this tool to extract size and morphology measurements of InP/ZnSe QDs. When compared with hand-drawn diameter measurements, the Fiji Particle Analysis Feret diameters were more accurate, more precise, and more reliable. Furthermore, the Fiji Particle Analysis offers quantitative morphological descriptors, such as solidity, that discerns changes in sample morphology that qualitative assessment cannot. This tool was used in a methodological study of ZnSe shelling parameters to assess the impact of each synthetic parameter on shell deposition. In this study shelling precursor injection rate, annealing temperature, and ligand identity were all varied independently. The combination of ensemble PL measurements and quantitative morphological assessment revealed a complex balance between parameters favoring shell growth vs. core protection during shelling. Parameters were optimized such that a 0.05 mL/min continuous injection at 340 °C with the sterically bulky trioctylamine produced the InP/ZnSe QDs with a 47% PLQY, 45 nm linewidth, and 95.585% shell solidity.

Overall, high quality thick shell InP/ZnSe QDs were produced with PLQYs ~40-50% and ~45-55 nm linewidths. The original synthesis was optimized to reduce InP oxidation, improve reproducibility, and control interfacial indium alloying. The presence of indium alloying at the core/shell interface was found to provide in gap trap states that reduce PLQY. A technique for extracting size and morphology measurements from HAADF-STEM images was adapted for nanocrystals. This quantitative morphological analysis was used to further optimize the zinc selenide shelling synthesis and reveal the impact of key shelling parameters on InP-based QD fluorescence and shell morphology.

5.2 Future Directions

High quality thick-shell InP/ZnSe QDs have been synthesized and characterized. However, industrial and aqueous applications require better photostability in air, water, and oxidizing environments. Zinc sulfide offers better photochemical stability than zinc selenide, but because of its large lattice mismatch with InP, zinc sulfide shells cannot effectively be applied directly to InP QDs. Instead, it has been shown in the literature that ZnSe can be used as an intermediary shell between the InP core and ZnS shell. InP/ZnSe/ZnS QDs with near-unity PLQYs in red, green, and blue emission wavelengths have been produced and implemented in solid-state lighting applications such as QLEDs. Yet, these QDs still display relatively wide ensemble emission linewidths and imperfect single particle photostability (i.e., PL blinking). For InP-based QDs to be applied in applications with more strenuous environments (i.e., high pump fluence, aqueous biological environments), the zinc chemistry for shelling must be tightly controlled to produce thick-shelled defect-free QDs. The knowledge gained from the ZnSe shelling methodological study detailed here can be used to inform and improve the ZnS shelling chemistry. Furthermore, the adapted Fiji Particle Analysis method can be used to perform a methodological study of ZnS shelling chemistry. Optimization of the ZnS shelling procedure will lead to the expansion of InP-based QDs into previously inaccessible applications, such as lasing and biological tracking.

Additionally, the InP QD synthesis still requires further optimization. It is well known that nanocrystal synthesis is riddled with reproducibility challenges. InP is no stranger to this phenomenon, in part due to its sensitivity to *in situ* oxidation. Additionally, the precursor conversion dynamics for InP QD synthesis have not been fully elucidated. It has been shown that long-chain indium-carboxylate precursors are prone to incomplete conversion during their synthesis. In this work, each indium myristate batch effected InP QD nucleation and growth

dynamics differently. Each batch produced InP QDs of different sizes and size distributions, yet within each batch InP QDs were consistently reproduced at the same size and size distribution. This indicates a variation between indium myristate batches that impacts the nanocrystal nucleation and growth dynamics. It has been shown that long-chain iron carboxylates can form clusters.[173] If the indium myristate precursor is also forming clusters, the presence of a mixture of cluster and monomer could alter the nucleation and growth dynamics produced by different indium myristate batches. Preliminary mass spectrometry measurements of an indium myristate sample shows species significantly larger than a single $InMy_3$ monomer but was unable to identify the exact structures of these species. (Appendix Figure A.4) Future experiments comparing the mass spectrometry profiles of different indium myristate batches and their effect on InP QD growth dynamics could reveal a key connection in InP QD nucleation and growth mechanisms.

APPENDIX A

Commented [CSM7]: APPENDIX

Citation	Publication Date	Core Material	Shell Material	Emission Peak (nm)	Emission Linewidth (nm)	Quantum Yield (%)	Phosphorous Source
Shen et al. *J Mater Chem C Mater* **2017**, *5* (32), 8243–8249.	7/18/17	In(Zn)P	ZnS	480	44	76%	TDMAP
Kim et al. *Chemistry of Materials* **2020**, *32* (7), 2795–2802.	3/19/20	In(Zn)P	ZnSe/ZnS	485	37	95%	TMSiP
Ramasamy et al. *Chemistry of Materials* **2017**, *29* (16), 6893–6899.	8/4/17	In(Zn)P	ZnSe/ZnS	488	35	44%	TMSiP
Van Avermaet et al. *ACS Nano* **2022**, *16* (6), 9701–9712.	6/16/22	In(Zn)P	ZnS	491	56	92%	TDEAP
Ramasamy et al. *Chemistry of Materials* **2017**, *29* (16), 6893–6899.	8/4/17	In(Zn)P	ZnSe/ZnS	515	36	67%	TMSiP
Van Avermaet et al. *ACS Nano* **2022**, *16* (6), 9701–9712.	6/16/22	In(Zn)P	ZnSe/ZnS	518	45	100%	TDEAP
Nemoto et al. *Nanoscale* **2022**, *14* (27), 9900–9909.	7/4/22	In(Zn)P	ZnS	523	36	70%	TMSiP
Jo et al. *Adv Opt Mater* **2021**, *9* (16), 2100427.	5/20/21	In(Zn)P	ZnSe/ZnS	525	37	97%	TDMAP
Lee et al. *ACS Appl Mater Interfaces* **2022**, *14* (10), 12479–12487.	3/3/22	In(Zn)P	ZnSe/ZnS	525	37	93%	TMSiP
Lee et al. *Nanoscale* **2019**, *11* (48), 23251–23258.	11/5/19	InP	ZnSe/ZnS	530	36	95%	TMSiP
Kim et al. *ACS Appl Nano Mater* **2019**, *2* (3), 1496–1504.	2/6/19	In(Zn)P	ZnSe	532	39	34%	TMSiP
Ramasamy et al. *Chemistry of Materials* **2018**, *30* (11), 3643–3647.	5/25/18	In(Zn)P	ZnSe/ZnS	533	37	65%	TMSiP
Li et al. *J Am Chem Soc* **2019**, *141* (16), 6448–6452.	4/9/19	InP	ZnSe/ZnS	535	35	90%	TMSiP
Park et al. *Small* **2022**, *18* (8), 2105492.	12/9/21	InP	ZnSe/ZnS	538	38	86%	TMSiP
Ramasamy et al. *Chemistry of Materials* **2017**, *29* (16), 6893–6899.	8/4/17	In(Zn)P	ZnSe/ZnS	540	38	71%	TMSiP
Ramasamy et al. *Chemistry of Materials* **2018**, *30* (11), 3643–3647.	5/25/18	In(Zn)P	ZnSe/ZnS	550	36	60%	TMSiP
Van Avermaet et al. *ACS Nano* **2022**, *16* (6), 9701–9712.	6/16/22	In(Zn)P	ZnSe/ZnS	552	53	87%	TDEAP
Shen et al. *J Mater Chem C Mater* **2021**, *9* (30), 9599–9609.	6/28/21	In(Zn)P	ZnSe/ZnS	569	38	82%	TMSiP
Ramasamy et al. *Chemistry of Materials* **2018**, *30* (11), 3643–3647.	5/25/18	In(Zn)P	ZnSe/ZnS	580	36	58%	TMSiP
Reid et al. *Nano Lett* **2018**, *18* (2), 709–716.	12/28/18	InP	ZnS	585	51	43%	TMSiP
Shen et al. *J Mater Chem C Mater* **2021**, *9* (30), 9599–9609.	6/28/21	In(Zn)P	ZnSe/ZnS	588	40	88%	TMSiP
Shen et al. *J Mater Chem C Mater* **2021**, *9* (30), 9599–9609.	6/28/21	In(Zn)P	ZnSe/ZnS	601	43	91%	TMSiP
Van Avermaet et al. *ACS Nano* **2022**, *16* (6), 9701–9712.	6/16/22	In(Zn)P	ZnSe/ZnS	607	46	95%	TDEAP

Ramasamy et al. *Chemistry of Materials* **2018**, *30* (11), 3643–3647.	5/25/18	In(Zn)P	ZnSe/ZnS	610	37	55%	TMSiP
Li et al. *J Am Chem Soc* **2019**, *141* (16), 6448–6452.	4/9/19	InP	ZnSe/ZnS	618	42	93%	TMSiP
Tessier et al. *Chemistry of Materials* **2015**, *27* (13), 4893–4898.	6/11/15	In(Zn)P	ZnS	620	56	60%	TDEAP
Reid et al. *Nano Lett* **2018**, *18* (2), 709–716.	12/28/18	InP	ZnSe	620	40	40%	TMSiP
Choi et al. *J Mater Chem C Mater* **2022**, *10* (6), 2213–2222.	1/10/22	In(Zn)P	ZnSe/ZnS	621	44	86%	TDMAP
Ramasamy et al. *Chemistry of Materials* **2018**, *30* (11), 3643–3647.	5/25/18	In(Zn)P	ZnSe/ZnS	625	39	45%	TMSiP
Chandrasekaran et al. *Nano Lett* **2017**, *17* (10), 6104–6109.	9/12/17	In(Zn)P	ZnSe	629	47	65%	TDEAP
Won et al. *Nature* **2019**, *575* (7784), 634–638.	11/27/19	InP	ZnSe/ZnS	630	35	100%	TMSiP
Kim et al. *Nano Lett* **2021**, *21* (5), 2111–2116.	2/26/21	InP	ZnSe/ZnS	630	35	90%	TMSiP
Shen et al. *J Mater Chem C Mater* **2021**, *9* (30), 9599–9609.	6/28/21	In(Zn)P	ZnSe/ZnS	630	45	94%	TMSiP

Figure A.1 List of the best performing InP-based QDs from recent publications (organized by increasing emission peak wavelength).

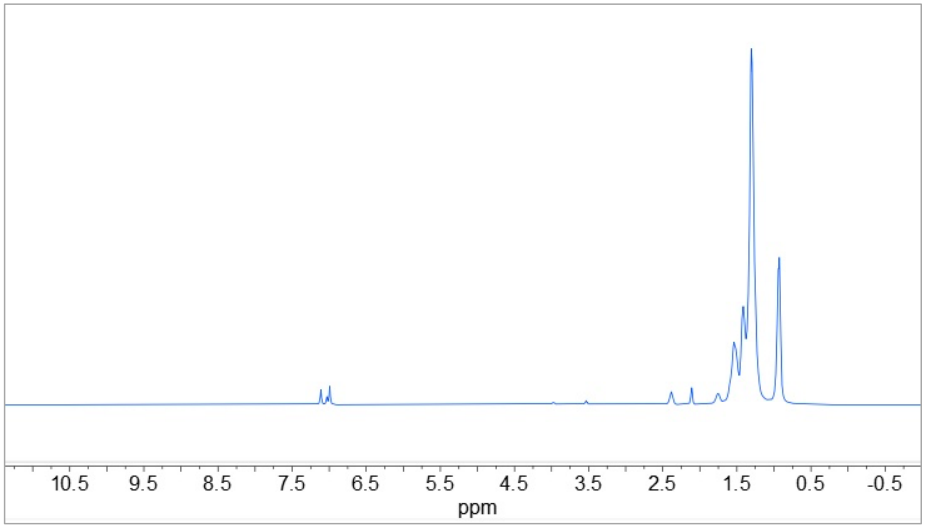

Figure A.2 ^{1}H NMR of synthesized indium myristate (8mM) in TOP 30 mM in d8 toluene. Alpha and beta carbons of indium myristate confirmed by peaks at 2.37 ppm and 1.74 ppm respectively. The large TOP peak covers all other relevant indium myristate chemical shifts.

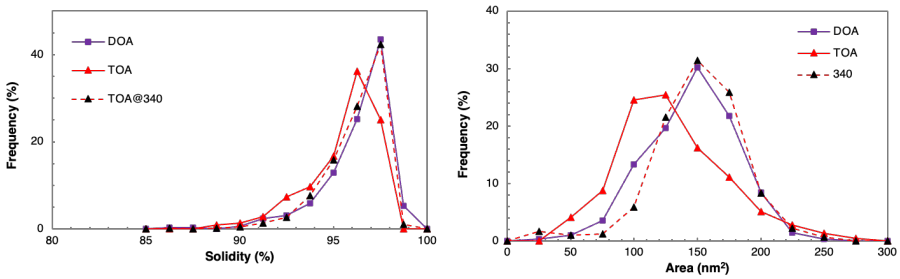

Figure A.3 ImageJ Particle Analysis measurements of InP/ZnSe QDs synthesized with dioctylamine (DOA) at 300 °C, trioctylamine (TOA) at 300 °C, and trioctylamine at 340 °C.

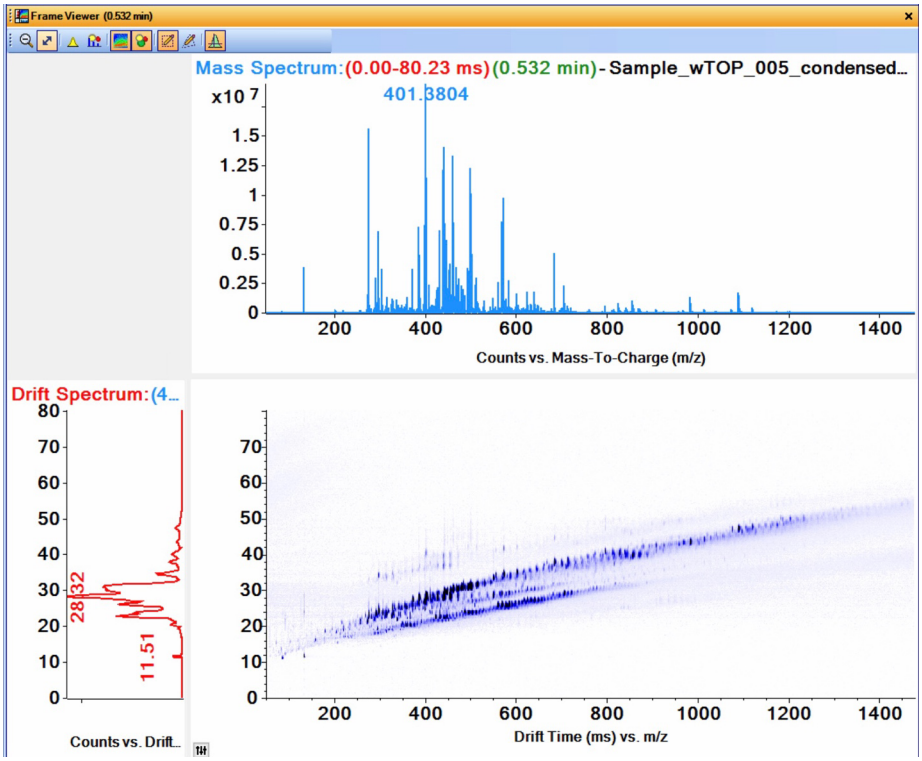

Figure A.4 Mass spectra for indium myristate. While most species are less than 796.88 m/z (the expected mass:charge ratio for a single $InMy_3$ monomer), the occurrence of significantly heavier species indicates the presence of indium myristate clusters.

REFERENCES

Commented [CSM8]: REFERENCES

(1) Bawendi, M. G.; Steigerwald, M. L.; Brus, L. E. The Quantum Mechanics of Larger Semiconductor Clusters ("Quantum Dots"). *Annu Rev Phys Chem* **1990**, *41*, 477–496.

(2) Brus, L. E. Electron–Electron and Electron-hole Interactions in Small Semiconductor Crystallites: The Size Dependence of the Lowest Excited Electronic State. *J Chem Phys* **1984**, *80* (9), 4403–4409. 10.1063/1.447218.

(3) Mićić, O. I.; Cheong, H. M.; Fu, H.; Zunger, A.; Sprague, J. R.; Mascarenhas, A.; Nozik, A. J. Size-Dependent Spectroscopy of InP Quantum Dots. *J Phys Chem B* **1997**, *101* (25), 4904–4912. 10.1021/jp9704731.

(4) Peng, X.; Wickham, J.; Alivisatos, A. P. Kinetics of II-VI and III-V Colloidal Semiconductor Nanocrystal Growth: "Focusing" of Size Distributions. *J Am Chem Soc* **1998**, *120* (21), 5343–5344. 10.1021/ja9805425.

(5) Medintz, I. L.; Uyeda, H. T.; Goldman, E. R.; Mattoussi, H. Quantum Dot Bioconjugates for Imaging, Labelling and Sensing. *Nat Mater* **2005**, *4* (6), 435–446. 10.1038/nmat1390.

(6) Thal, L. B.; Mann, V. R.; Sprinzen, D.; McBride, J. R.; Reid, K. R.; Tomlinson, I. D.; McMahon, D. G.; Cohen, B. E.; Rosenthal, S. J. Ligand-Conjugated Quantum Dots for Fast Sub-Diffraction Protein Tracking in Acute Brain Slices. *Biomater Sci* **2020**, *8* (3), 837–845. 10.1039/C9BM01629E.

(7) Fan, F.; Voznyy, O.; Sabatini, R. P.; Bicanic, K. T.; Adachi, M. M.; McBride, J. R.; Reid, K. R.; Park, Y.-S.; Li, X.; Jain, A.; Quintero-Bermudez, R.; Saravanapavanantham, M.; Liu, M.; Korkusinski, M.; Hawrylak, P.; Klimov, V. I.; Rosenthal, S. J.; Hoogland, S.; Sargent, E. H. Continuous-Wave Lasing in Colloidal Quantum Dot Solids Enabled by Facet-Selective Epitaxy. *Nature* **2017**, *544*, 75.

(8) Hanifi, D. A.; Bronstein, N. D.; Koscher, B. A.; Nett, Z.; Swabeck, J. K.; Takano, K.; Schwartzberg, A. M.; Maserati, L.; Vandewal, K.; van de Burgt, Y.; Salleo, A.; Alivisatos, A. P. Redefining Near-Unity Luminescence in Quantum Dots with Photothermal Threshold Quantum Yield. *Science (1979)* **2019**, *363* (6432), 1199–1202. 10.1126/science.aat3803.

(9) Park, Y.-S.; Roh, J.; Diroll, B. T.; Schaller, R. D.; Klimov, V. I. Colloidal Quantum Dot Lasers. *Nat Rev Mater* **2021**, *6* (5), 382–401. 10.1038/s41578-020-00274-9.

(10) Schreuder, M. A.; Xiao, K.; Ivanov, I. N.; Weiss, S. M.; Rosenthal, S. J. White Light-Emitting Diodes Based on Ultrasmall CdSe Nanocrystal Electroluminescence. *Nano Lett* **2010**, *10* (2), 573–576. 10.1021/nl903515g.

(11) Shirasaki, Y.; Supran, G. J.; Bawendi, M. G.; Bulović, V. Emergence of Colloidal Quantum-Dot Light-Emitting Technologies. *Nat Photonics* **2013**, *7* (1), 13–23. 10.1038/nphoton.2012.328.

(12) Dai, X.; Zhang, Z.; Jin, Y.; Niu, Y.; Cao, H.; Liang, X.; Chen, L.; Wang, J.; Peng, X. Solution-Processed, High-Performance Light-Emitting Diodes Based on Quantum Dots. *Nature* **2014**, *515* (7525), 96–99. 10.1038/nature13829.

(13) Manders, J. R.; Qian, L.; Titov, A.; Hyvonen, J.; Tokarz-Scott, J.; Acharya, K. P.; Yang, Y.; Cao, W.; Zheng, Y.; Xue, J.; Holloway, P. H. High Efficiency and Ultra-Wide Color Gamut Quantum Dot LEDs for next Generation Displays. *J Soc Inf Disp* **2015**, *23* (11), 523–528. https://doi.org/10.1002/jsid.393.

(14) Won, Y.-H.; Cho, O.; Kim, T.; Chung, D.-Y.; Kim, T.; Chung, H.; Jang, H.; Lee, J.; Kim, D.; Jang, E. Highly Efficient and Stable InP/ZnSe/ZnS Quantum Dot Light-Emitting Diodes. *Nature* **2019**, *575* (7784), 634–638. 10.1038/s41586-019-1771-5.

(15) Aharonovich, I.; Englund, D.; Toth, M. Solid-State Single-Photon Emitters. *Nat Photonics* **2016**, *10* (10), 631–641. 10.1038/nphoton.2016.186.

(16) Wang, L.; Lin, J.; Hu, Y.; Guo, X.; Lv, Y.; Tang, Z.; Zhao, J.; Fan, Y.; Zhang, N.; Wang, Y.; Liu, X. Blue Quantum Dot Light-Emitting Diodes with High Electroluminescent Efficiency. *ACS Appl Mater Interfaces* **2017**, *9* (44), 38755–38760. 10.1021/acsami.7b10785.

(17) Rossetti, R.; Brus, L. Electron-Hole Recombination Emission as a Probe of Surface Chemistry in Aqueous Cadmium Sulfide Colloids. *J Phys Chem* **1982**, *86* (23), 4470–4472. 10.1021/j100220a003.

(18) Rossetti, R.; Nakahara, S.; Brus, L. E. Quantum Size Effects in the Redox Potentials, Resonance Raman Spectra, and Electronic Spectra of CdS Crystallites in Aqueous Solution. *J Chem Phys* **1983**, *79* (2), 1086–1088. 10.1063/1.445834.

(19) Brus, L. E. A Simple Model for the Ionization Potential, Electron Affinity, and Aqueous Redox Potentials of Small Semiconductor Crystallites. *J Chem Phys* **1983**, *79* (11), 5566–5571. 10.1063/1.445676.

(20) Nenadovic, M. T.; Rajh, T.; Micic, O. I. Size Quantization in Small Semiconductor Particles. *J Phys Chem* **1985**, *89* (3), 397–399. 10.1021/j100249a004.

(21) Nedeljkovic, J. M.; Nenadovic, M. T.; Micic, O. I.; Nozik, A. J. Enhanced Photoredox Chemistry in Quantized Semiconductor Colloids. *J Phys Chem* **1986**, *90* (1), 12–13. 10.1021/j100273a005.

(22) Brus, L. Electronic Wave Functions in Semiconductor Clusters: Experiment and Theory. *J Phys Chem* **1986**, *90* (12), 2555–2560. 10.1021/j100403a003.

(23) Micic, O. I.; Curtis, C. J.; Jones, K. M.; Sprague, J. R.; Nozik, A. J. Synthesis and Characterization of InP Quantum Dots. *J Phys Chem* **1994**, *98* (19), 4966–4969. 10.1021/j100070a004.

(24) Douglas, T.; Theopold, K. H. Molecular Precursors for Indium Phosphide and Synthesis of Small III-V Semiconductor Clusters in Solution. *Inorg Chem* **1991**, *30* (4), 594–596. 10.1021/ic00004a002.

(25) Derfus, A. M.; Chan, W. C. W.; Bhatia, S. N. Probing the Cytotoxicity of Semiconductor Quantum Dots. *Nano Lett* **2004**, *4* (1), 11–18. 10.1021/nl0347334.

(26) *Annex XVII to REACH-Conditions of Restriction. Entry 23.*; 2011. https://echa.europa.eu/documents/10162/3bfef8a3-8c97-4d85-ae0b-ac6827de49a9 (accessed 2023-01-01).

(27) Ron, H. A Toxicologic Review of Quantum Dots: Toxicity Depends on Physicochemical and Environmental Factors. *Environ Health Perspect* **2006**, *114* (2), 165–172. 10.1289/ehp.8284.

(28) Brunetti, V.; Chibli, H.; Fiammengo, R.; Galeone, A.; Malvindi, M. A.; Vecchio, G.; Cingolani, R.; Nadeau, J. L.; Pompa, P. P. InP/ZnS as a Safer Alternative to CdSe/ZnS Core/Shell Quantum Dots: In Vitro and in Vivo Toxicity Assessment. *Nanoscale* **2013**, *5* (1), 307–317. 10.1039/C2NR33024E.

(29) *CRC Handbook of Chemistry and Physics*, 102nd ed.; Rumble, J., Ed.; CRC Press, 2021.

(30) Kim, Y.; Chang, J. H.; Choi, H.; Kim, Y.-H.; Bae, W. K.; Jeong, S. III–V Colloidal Nanocrystals: Control of Covalent Surfaces. *Chem Sci* **2020**, *11* (4), 913–922. 10.1039/C9SC04290C.

(31) Li, L.; Reiss, P. One-Pot Synthesis of Highly Luminescent InP/ZnS Nanocrystals without Precursor Injection. *J Am Chem Soc* **2008**, *130* (35), 11588–11589. 10.1021/ja803687e.

(32) Li, Y.; Hou, X.; Dai, X.; Yao, Z.; Lv, L.; Jin, Y.; Peng, X. Stoichiometry-Controlled InP-Based Quantum Dots: Synthesis, Photoluminescence, and Electroluminescence. *J Am Chem Soc* **2019**, *141* (16), 6448–6452. 10.1021/jacs.8b12908.

(33) Kim, Y.; Ham, S.; Jang, H.; Min, J. H.; Chung, H.; Lee, J.; Kim, D.; Jang, E. Bright and Uniform Green Light Emitting InP/ZnSe/ZnS Quantum Dots for Wide Color Gamut Displays. *ACS Appl Nano Mater* **2019**, *2* (3), 1496–1504. 10.1021/acsanm.8b02063.

(34) Chandrasekaran, V.; Tessier, M. D.; Dupont, D.; Geiregat, P.; Hens, Z.; Brainis, E. Nearly Blinking-Free, High-Purity Single-Photon Emission by Colloidal InP/ZnSe Quantum Dots. *Nano Lett* **2017**, *17* (10), 6104–6109. 10.1021/acs.nanolett.7b02634.

(35) Reid, K. R.; McBride, J. R.; Freymeyer, N. J.; Thal, L. B.; Rosenthal, S. J. Chemical Structure, Ensemble and Single-Particle Spectroscopy of Thick-Shell InP–ZnSe Quantum Dots. *Nano Lett* **2018**, *18* (2), 709–716. 10.1021/acs.nanolett.7b03703.

(36) Chen, B.; Li, D.; Wang, F. InP Quantum Dots: Synthesis and Lighting Applications. *Small* **2020**, *16* (32), 2002454. 10.1002/smll.202002454.

(37) Tamang, S.; Lincheneau, C.; Hermans, Y.; Jeong, S.; Reiss, P. Chemistry of InP Nanocrystal Syntheses. *Chemistry of Materials* **2016**, *28* (8), 2491–2506. 10.1021/acs.chemmater.5b05044.

(38) Xie, L.; Shen, Y.; Franke, D.; Sebastián, V.; Bawendi, M. G.; Jensen, K. F. Characterization of Indium Phosphide Quantum Dot Growth Intermediates Using MALDI-TOF Mass Spectrometry. *J Am Chem Soc* **2016**, *138* (41), 13469–13472. 10.1021/jacs.6b06468.

(39) Siramdas, R.; McLaurin, E. J. InP Nanocrystals with Color-Tunable Luminescence by Microwave-Assisted Ionic-Liquid Etching. *Chemistry of Materials* **2017**, *29* (5), 2101–2109. 10.1021/acs.chemmater.6b04457.

(40) Xu, Z.; Li, Y.; Li, J.; Pu, C.; Zhou, J.; Lv, L.; Peng, X. Formation of Size-Tunable and Nearly Monodisperse InP Nanocrystals: Chemical Reactions and Controlled Synthesis. *Chemistry of Materials* **2019**, *31* (14), 5331–5341. 10.1021/acs.chemmater.9b02292.

(41) Park, J.; Won, Y.; Han, Y.; Kim, H.; Jang, E.; Kim, D. Tuning Hot Carrier Dynamics of InP/ZnSe/ZnS Quantum Dots by Shell Morphology Control. *Small* **2022**, *18* (8), 2105492. 10.1002/smll.202105492.

(42) Park, N.; Eagle, F. W.; DeLarme, A. J.; Monahan, M.; LoCurto, T.; Beck, R.; Li, X.; Cossairt, B. M. Tuning the Interfacial Stoichiometry of InP Core and InP/ZnSe Core/Shell Quantum Dots. *J Chem Phys* **2021**, *155* (8), 084701. 10.1063/5.0060462.

(43) Laufersky, G.; Bradley, S.; Frecaut, E.; Lein, M.; Nann, T. Unraveling Aminophosphine Redox Mechanisms for Glovebox-Free InP Quantum Dot Syntheses. *Nanoscale* **2018**, *10* (18), 8752–8762. 10.1039/C8NR01286E.

(44) Choi, S.-W.; Kim, H.-M.; Yoon, S.-Y.; Jo, D.-Y.; Kim, S.-K.; Kim, Y.; Park, S. M.; Lee, Y.-J.; Yang, H. Aminophosphine-Derived, High-Quality Red-Emissive InP Quantum Dots by the Use of an Unconventional in Halide. *J Mater Chem C Mater* **2022**, *10* (6), 2213–2222. 10.1039/D1TC06072D.

(45) Baquero, E. A.; Virieux, H.; Swain, R. A.; Gillet, A.; Cros-Gagneux, A.; Coppel, Y.; Chaudret, B.; Nayral, C.; Delpech, F. Synthesis of Oxide-Free InP Quantum Dots: Surface Control and H2-Assisted Growth. *Chemistry of Materials* **2017**, *29* (22), 9623–9627. 10.1021/acs.chemmater.7b04069.

(46) Shen, C.; Zhu, Y.; Li, Z.; Li, J.; Tao, H.; Zou, J.; Xu, X.; Xu, G. Highly Luminescent InP–In(Zn)P/ZnSe/ZnS Core/Shell/Shell Colloidal Quantum Dots with Tunable Emissions Synthesized Based on Growth-Doping. *J Mater Chem C Mater* **2021**, *9* (30), 9599–9609. 10.1039/D1TC01664D.

(47) Thomas, A.; Sandeep, K.; Somasundaran, S. M.; Thomas, K. G. How Trap States Affect Charge Carrier Dynamics of CdSe and InP Quantum Dots: Visualization through Complexation with Viologen. *ACS Energy Lett* **2018**, *3* (10), 2368–2375. 10.1021/acsenergylett.8b01532.

(48) Battaglia, D.; Peng, X. Formation of High Quality InP and InAs Nanocrystals in a Noncoordinating Solvent. *Nano Lett* **2002**, *2* (9), 1027–1030. 10.1021/nl025687v.

(49) Song, W.-S.; Lee, H.-S.; Lee, J. C.; Jang, D. S.; Choi, Y.; Choi, M.; Yang, H. Amine-Derived Synthetic Approach to Color-Tunable InP/ZnS Quantum Dots with High Fluorescent Qualities. *Journal of Nanoparticle Research* **2013**, *15* (6), 1750. 10.1007/s11051-013-1750-y.

(50) Jo, J.; Jo, D.; Choi, S.; Lee, S.; Kim, H.; Yoon, S.; Kim, Y.; Han, J.; Yang, H. Highly Bright, Narrow Emissivity of InP Quantum Dots Synthesized by Aminophosphine: Effects of Double Shelling Scheme and Ga Treatment. *Adv Opt Mater* **2021**, *9* (16), 2100427. 10.1002/adom.202100427.

(51) McMurtry, B. M.; Qian, K.; Teglasi, J. K.; Swarnakar, A. K.; de Roo, J.; Owen, J. S. Continuous Nucleation and Size Dependent Growth Kinetics of Indium Phosphide Nanocrystals. *Chemistry of Materials* **2020**, *32* (10), 4358–4368. 10.1021/acs.chemmater.0c01561.

(52) Li, L.; Protière, M.; Reiss, P. Economic Synthesis of High Quality InP Nanocrystals Using Calcium Phosphide as the Phosphorus Precursor. *Chemistry of Materials* **2008**, *20* (8), 2621–2623. 10.1021/cm7035579.

(53) Huang, K.; Demadrille, R.; Silly, M. G.; Sirotti, F.; Reiss, P.; Renault, O. Internal Structure of InP/ZnS Nanocrystals Unraveled by High-Resolution Soft X-Ray Photoelectron Spectroscopy. *ACS Nano* **2010**, *4* (8), 4799–4805. 10.1021/nn100581t.

(54) Gary, D. C.; Cossairt, B. M. Role of Acid in Precursor Conversion During InP Quantum Dot Synthesis. *Chemistry of Materials* **2013**, *25* (12), 2463–2469. 10.1021/cm401289j.

(55) Zan, F.; Ren, J. Gas-Liquid Phase Synthesis of Highly Luminescent InP/ZnS Core/Shell Quantum Dots Using Zinc Phosphide as a New Phosphorus Source. *J Mater Chem* **2012**, *22* (5), 1794–1799. 10.1039/C1JM13982G.

(56) Liu, Z.; Kumbhar, A.; Xu, D.; Zhang, J.; Sun, Z.; Fang, J. Coreduction Colloidal Synthesis of III–V Nanocrystals: The Case of InP. *Angewandte Chemie International Edition* **2008**, *47* (19), 3540–3542. 10.1002/anie.200800281.

(57) Gary, D. C.; Glassy, B. A.; Cossairt, B. M. Investigation of Indium Phosphide Quantum Dot Nucleation and Growth Utilizing Triarylsilylphosphine Precursors. *Chemistry of Materials* **2014**, *26* (4), 1734–1744. 10.1021/cm500102q.

(58) Harris, D. K.; Bawendi, M. G. Improved Precursor Chemistry for the Synthesis of III–V Quantum Dots. *J Am Chem Soc* **2012**, *134* (50), 20211–20213. 10.1021/ja309863n.

(59) Yu, P.; Shan, Y.; Cao, S.; Hu, Y.; Li, Q.; Zeng, R.; Zou, B.; Wang, Y.; Zhao, J. Inorganic Solid Phosphorus Precursor of Sodium Phosphaethynolate for Synthesis of Highly Luminescent InP-Based Quantum Dots. *ACS Energy Lett* **2021**, *6* (8), 2697–2703. 10.1021/acsenergylett.1c01067.

(60) Tessier, M. D.; Dupont, D.; de Nolf, K.; de Roo, J.; Hens, Z. Economic and Size-Tunable Synthesis of InP/ZnE (E = S, Se) Colloidal Quantum Dots. *Chemistry of Materials* **2015**, *27* (13), 4893–4898. 10.1021/acs.chemmater.5b02138.

(61) Shen, W.; Tang, H.; Yang, X.; Cao, Z.; Cheng, T.; Wang, X.; Tan, Z.; You, J.; Deng, Z. Synthesis of Highly Fluorescent InP/ZnS Small-Core/Thick-Shell Tetrahedral-Shaped Quantum Dots for Blue Light-Emitting Diodes. *J Mater Chem C Mater* **2017**, *5* (32), 8243–8249. 10.1039/C7TC02927F.

(62) Ramasamy, P.; Kim, N.; Kang, Y.-S.; Ramirez, O.; Lee, J.-S. Tunable, Bright, and Narrow-Band Luminescence from Colloidal Indium Phosphide Quantum Dots. *Chemistry of Materials* **2017**, *29* (16), 6893–6899. 10.1021/acs.chemmater.7b02204.

(63) Cui, Z.; Mei, S.; Wen, Z.; Yang, D.; Qin, S.; Xiong, Z.; Yang, B.; He, H.; Bao, R.; Qiu, Y.; Chen, Y.; Zhang, W.; Xie, F.; Xing, G.; Guo, R. Synergistic Effect of Halogen Ions and Shelling Temperature on Anion Exchange Induced Interfacial Restructuring for Highly Efficient Blue Emissive InP/ZnS Quantum Dots. *Small* **2022**, *18* (15), 2108120. 10.1002/smll.202108120.

(64) Gary, D. C.; Petrone, A.; Li, X.; Cossairt, B. M. Investigating the Role of Amine in InP Nanocrystal Synthesis: Destabilizing Cluster Intermediates by Z-Type Ligand Displacement. *Chemical Communications* **2017**, *53* (1), 161–164. 10.1039/C6CC07952K.

(65) Ritchhart, A.; Cossairt, B. M. Templated Growth of InP Nanocrystals with a Polytwistane Structure. *Angewandte Chemie International Edition* **2018**, *57* (7), 1908–1912. 10.1002/anie.201711539.

(66) Shen, Y.; Roberge, A.; Tan, R.; Gee, M. Y.; Gary, D. C.; Huang, Y.; Blom, D. A.; Benicewicz, B. C.; Cossairt, B. M.; Greytak, A. B. Gel Permeation Chromatography as a Multifunctional Processor for Nanocrystal Purification and On-Column Ligand Exchange Chemistry. *Chem Sci* **2016**, *7* (9), 5671–5679. 10.1039/C6SC01301E.

(67) Roberge, A.; Stein, J. L.; Shen, Y.; Cossairt, B. M.; Greytak, A. B. Purification and In Situ Ligand Exchange of Metal-Carboxylate-Treated Fluorescent InP Quantum Dots via Gel Permeation Chromatography. *J Phys Chem Lett* **2017**, *8* (17), 4055–4060. 10.1021/acs.jpclett.7b01772.

(68) Nguyen, H. A.; Dou, F. Y.; Park, N.; Wu, S.; Sarsito, H.; Diakubama, B.; Larson, H.; Nishiwaki, E.; Homer, M.; Cash, M.; Cossairt, B. M. Predicting Indium Phosphide Quantum Dot Properties from Synthetic Procedures Using Machine Learning. *Chemistry of Materials* **2022**, *34* (14), 6296–6311. 10.1021/acs.chemmater.2c00640.

(69) Cao, F.; Wang, S.; Wang, F.; Wu, Q.; Zhao, D.; Yang, X. A Layer-by-Layer Growth Strategy for Large-Size InP/ZnSe/ZnS Core–Shell Quantum Dots Enabling High-Efficiency Light-Emitting Diodes. *Chemistry of Materials* **2018**, *30* (21), 8002–8007. 10.1021/acs.chemmater.8b03671.

(70) Achorn, O. B.; Franke, D.; Bawendi, M. G. Seedless Continuous Injection Synthesis of Indium Phosphide Quantum Dots as a Route to Large Size and Low Size Dispersity. *Chemistry of Materials* **2020**, *32* (15), 6532–6539. 10.1021/acs.chemmater.0c01906.

(71) Zhang, X.; Hudson, M. H.; Castellano, F. N. Engineering Long-Lived Blue Photoluminescence from InP Quantum Dots Using Isomers of Naphthoic Acid. *J Am Chem Soc* **2022**, *144* (8), 3527–3534. 10.1021/jacs.1c12207.

(72) Gary, D. C.; Terban, M. W.; Billinge, S. J. L.; Cossairt, B. M. Two-Step Nucleation and Growth of InP Quantum Dots via Magic-Sized Cluster Intermediates. *Chemistry of Materials* **2015**, *27* (4), 1432–1441. 10.1021/acs.chemmater.5b00286.

(73) Hughes, K. E.; Stein, J. L.; Friedfeld, M. R.; Cossairt, B. M.; Gamelin, D. R. Effects of Surface Chemistry on the Photophysics of Colloidal InP Nanocrystals. *ACS Nano* **2019**, *13* (12), 14198–14207. 10.1021/acsnano.9b07027.

(74) Ramasamy, P.; Ko, K.-J.; Kang, J.-W.; Lee, J.-S. Two-Step "Seed-Mediated" Synthetic Approach to Colloidal Indium Phosphide Quantum Dots with High-Purity Photo- and Electroluminescence. *Chemistry of Materials* **2018**, *30* (11), 3643–3647. 10.1021/acs.chemmater.8b02049.

(75) Kim, K.; Suh, Y.-H.; Kim, D.; Choi, Y.; Bang, E.; Kim, B. H.; Park, J. Zinc Oxo Clusters Improve the Optoelectronic Properties on Indium Phosphide Quantum Dots. *Chemistry of Materials* **2020**, *32* (7), 2795–2802. 10.1021/acs.chemmater.9b04309.

(76) Kim, K.; Yoo, D.; Choi, H.; Tamang, S.; Ko, J.-H.; Kim, S.; Kim, Y.-H.; Jeong, S. Halide–Amine Co-Passivated Indium Phosphide Colloidal Quantum Dots in Tetrahedral Shape. *Angewandte Chemie International Edition* **2016**, *55* (11), 3714–3718. 10.1002/anie.201600289.

(77) Stein, J. L.; Holden, W. M.; Venkatesh, A.; Mundy, M. E.; Rossini, A. J.; Seidler, G. T.; Cossairt, B. M. Probing Surface Defects of InP Quantum Dots Using Phosphorus Kα and Kβ X-Ray Emission Spectroscopy. *Chemistry of Materials* **2018**, *30* (18), 6377–6388. 10.1021/acs.chemmater.8b02590.

(78) Kim, Y.; Choi, H.; Lee, Y.; Koh, W.; Cho, E.; Kim, T.; Kim, H.; Kim, Y.-H.; Jeong, H. Y.; Jeong, S. Tailored Growth of Single-Crystalline InP Tetrapods. *Nat Commun* **2021**, *12* (1), 4454. 10.1038/s41467-021-24765-7.

(79) Kim, T.; Kim, Y.; Park, S.; Park, K.; Wang, Z.; Oh, S. H.; Jeong, S.; Kim, D. Shape-Tuned Multiphoton-Emitting InP Nanotetrapods. *Advanced Materials* **2022**, *34* (19), 2110665. 10.1002/adma.202110665.

(80) Polte, J. Fundamental Growth Principles of Colloidal Metal Nanoparticles – a New Perspective. *CrystEngComm* **2015**, *17* (36), 6809–6830. 10.1039/C5CE01014D.

(81) Becker, R.; Döring, W. Kinetische Behandlung Der Keimbildung in Übersättigten Dämpfen. *Ann Phys* **1935**, *416* (8), 719–752. https://doi.org/10.1002/andp.19354160806.

(82) Gary, D. C.; Flowers, S. E.; Kaminsky, W.; Petrone, A.; Li, X.; Cossairt, B. M. Single-Crystal and Electronic Structure of a 1.3 Nm Indium Phosphide Nanocluster. *J Am Chem Soc* **2016**, *138* (5), 1510–1513. 10.1021/jacs.5b13214.

(83) Friedfeld, M. R.; Stein, J. L.; Cossairt, B. M. Main-Group-Semiconductor Cluster Molecules as Synthetic Intermediates to Nanostructures. *Inorg Chem* **2017**, *56* (15), 8689–8697. 10.1021/acs.inorgchem.7b00291.

(84) Friedfeld, M. R.; Johnson, D. A.; Cossairt, B. M. Conversion of InP Clusters to Quantum Dots. *Inorg Chem* **2019**, *58* (1), 803–810. 10.1021/acs.inorgchem.8b02945.

(85) Cros-Gagneux, A.; Delpech, F.; Nayral, C.; Cornejo, A.; Coppel, Y.; Chaudret, B. Surface Chemistry of InP Quantum Dots: A Comprehensive Study. *J Am Chem Soc* **2010**, *132* (51), 18147–18157. 10.1021/ja104673y.

(86) Narayanaswamy, A.; Xu, H.; Pradhan, N.; Kim, M.; Peng, X. Formation of Nearly Monodisperse In2O3 Nanodots and Oriented-Attached Nanoflowers: Hydrolysis and Alcoholysis vs Pyrolysis. *J Am Chem Soc* **2006**, *128* (31), 10310–10319. 10.1021/ja0627601.

(87) Kirkwood, N.; de Backer, A.; Altantzis, T.; Winckelmans, N.; Longo, A.; Antolinez, F. v; Rabouw, F. T.; de Trizio, L.; Geuchies, J. J.; Mulder, J. T.; Renaud, N.; Bals, S.; Manna, L.; Houtepen, A. J. Locating and Controlling the Zn Content in In(Zn)P Quantum Dots. *Chemistry of Materials* **2020**, *32* (1), 557–565. 10.1021/acs.chemmater.9b04407.

(88) Xie, R.; Battaglia, D.; Peng, X. Colloidal InP Nanocrystals as Efficient Emitters Covering Blue to Near-Infrared. *J Am Chem Soc* **2007**, *129* (50), 15432–15433. 10.1021/ja076363h.

(89) Peter M., A.; Brian J., W.; Bawendi, M. G. Mechanistic Insights into the Formation of InP Quantum Dots. *Angewandte Chemie International Edition* **2010**, *49* (4), 760–762. 10.1002/anie.200905632.

(90) Calvin, J. J.; O'Brien, E. A.; Sedlak, A. B.; Balan, A. D.; Alivisatos, A. P. Thermodynamics of Composition Dependent Ligand Exchange on the Surfaces of Colloidal Indium Phosphide Quantum Dots. *ACS Nano* **2021**, *15* (1), 1407–1420. 10.1021/acsnano.0c08683.

(91) Sluydts, M.; de Nolf, K.; van Speybroeck, V.; Cottenier, S.; Hens, Z. Ligand Addition Energies and the Stoichiometry of Colloidal Nanocrystals. *ACS Nano* **2016**, *10* (1), 1462–1474. 10.1021/acsnano.5b06965.

(92) Ritchhart, A.; Cossairt, B. M. Quantifying Ligand Exchange on InP Using an Atomically Precise Cluster Platform. *Inorg Chem* **2019**, *58* (4), 2840–2847. 10.1021/acs.inorgchem.8b03524.

(93) Toufanian, R.; Piryatinski, A.; Mahler, A. H.; Iyer, R.; Hollingsworth, J. A.; Dennis, A. M. Bandgap Engineering of Indium Phosphide-Based Core/Shell Heterostructures Through Shell Composition and Thickness. *Frontiers in Chemistry*. 2018, p 567. https://www.frontiersin.org/article/10.3389/fchem.2018.00567.

(94) Calvin, J. J.; Swabeck, J. K.; Sedlak, A. B.; Kim, Y.; Jang, E.; Alivisatos, A. P. Thermodynamic Investigation of Increased Luminescence in Indium Phosphide Quantum Dots by Treatment with Metal Halide Salts. *J Am Chem Soc* **2020**, *142* (44), 18897–18906. 10.1021/jacs.0c08954.

(95) Protière, M.; Reiss, P. Amine-Induced Growth of an In2O3 Shell on Colloidal InP Nanocrystals. *Chemical Communications* **2007**, No. 23, 2417–2419. 10.1039/B701092C.

(96) Virieux, H.; le Troedec, M.; Cros-Gagneux, A.; Ojo, W.-S.; Delpech, F.; Nayral, C.; Martinez, H.; Chaudret, B. InP/ZnS Nanocrystals: Coupling NMR and XPS for Fine Surface

and Interface Description. *J Am Chem Soc* **2012**, *134* (48), 19701–19708. 10.1021/ja307124m.

(97) Tessier, M. D.; Baquero, E. A.; Dupont, D.; Grigel, V.; Bladt, E.; Bals, S.; Coppel, Y.; Hens, Z.; Nayral, C.; Delpech, F. Interfacial Oxidation and Photoluminescence of InP-Based Core/Shell Quantum Dots. *Chemistry of Materials* **2018**, *30* (19), 6877–6883. 10.1021/acs.chemmater.8b03117.

(98) Xie, L.; Harris, D. K.; Bawendi, M. G.; Jensen, K. F. Effect of Trace Water on the Growth of Indium Phosphide Quantum Dots. *Chemistry of Materials* **2015**, *27* (14), 5058–5063. 10.1021/acs.chemmater.5b01626.

(99) Ramasamy, P.; Kim, B.; Lee, M.-S.; Lee, J.-S. Beneficial Effects of Water in the Colloidal Synthesis of InP/ZnS Core–Shell Quantum Dots for Optoelectronic Applications. *Nanoscale* **2016**, *8* (39), 17159–17168. 10.1039/C6NR04713K.

(100) Vikram, A.; Zahid, A.; Bhargava, S. S.; Keating, L. P.; Sutrisno, A.; Khare, A.; Trefonas, P.; Shim, M.; Kenis, P. J. A. Mechanistic Insights into Size-Focused Growth of Indium Phosphide Nanocrystals in the Presence of Trace Water. *Chemistry of Materials* **2020**, *32* (8), 3577–3584. 10.1021/acs.chemmater.0c00781.

(101) van Avermaet, H.; Schiettecatte, P.; Hinz, S.; Giordano, L.; Ferrari, F.; Nayral, C.; Delpech, F.; Maultzsch, J.; Lange, H.; Hens, Z. Full-Spectrum InP-Based Quantum Dots with Near-Unity Photoluminescence Quantum Efficiency. *ACS Nano* **2022**, *16* (6), 9701–9712. 10.1021/acsnano.2c03138.

(102) Janke, E. M.; Williams, N. E.; She, C.; Zherebetskyy, D.; Hudson, M. H.; Wang, L.; Gosztola, D. J.; Schaller, R. D.; Lee, B.; Sun, C.; Engel, G. S.; Talapin, D. v. Origin of Broad Emission Spectra in InP Quantum Dots: Contributions from Structural and Electronic Disorder. *J Am Chem Soc* **2018**, *140* (46), 15791–15803. 10.1021/jacs.8b08753.

(103) Mićić, O. I.; Sprague, J.; Lu, Z.; Nozik, A. J. Highly Efficient Band-edge Emission from InP Quantum Dots. *Appl Phys Lett* **1996**, *68* (22), 3150–3152. 10.1063/1.115807.

(104) Adam, S.; Talapin, D. v; Borchert, H.; Lobo, A.; McGinley, C.; de Castro, A. R. B.; Haase, M.; Weller, H.; Möller, T. The Effect of Nanocrystal Surface Structure on the Luminescence Properties: Photoemission Study of HF-Etched InP Nanocrystals. *J Chem Phys* **2005**, *123* (8), 084706. 10.1063/1.2004901.

(105) Talapin, D. v; Gaponik, N.; Borchert, H.; Rogach, A. L.; Haase, M.; Weller, H. Etching of Colloidal InP Nanocrystals with Fluorides: Photochemical Nature of the Process Resulting in High Photoluminescence Efficiency. *J Phys Chem B* **2002**, *106* (49), 12659–12663. 10.1021/jp026380n.

(106) Kim, T.-G.; Zherebetskyy, D.; Bekenstein, Y.; Oh, M. H.; Wang, L.-W.; Jang, E.; Alivisatos, A. P. Trap Passivation in Indium-Based Quantum Dots through Surface Fluorination: Mechanism and Applications. *ACS Nano* **2018**, *12* (11), 11529–11540. 10.1021/acsnano.8b06692.

(107) Stein, J. L.; Mader, E. A.; Cossairt, B. M. Luminescent InP Quantum Dots with Tunable Emission by Post-Synthetic Modification with Lewis Acids. *J Phys Chem Lett* **2016**, *7* (7), 1315–1320. 10.1021/acs.jpclett.6b00177.

(108) Pietra, F.; de Trizio, L.; Hoekstra, A. W.; Renaud, N.; Prato, M.; Grozema, F. C.; Baesjou, P. J.; Koole, R.; Manna, L.; Houtepen, A. J. Tuning the Lattice Parameter of InxZnyP for Highly Luminescent Lattice-Matched Core/Shell Quantum Dots. *ACS Nano* **2016**, *10* (4), 4754–4762. 10.1021/acsnano.6b01266.

(109) Friedfeld, M. R.; Stein, J. L.; Johnson, D. A.; Park, N.; Henry, N. A.; Enright, M. J.; Mocatta, D.; Cossairt, B. M. Effects of Zn2+ and Ga3+ Doping on the Quantum Yield of Cluster-Derived InP Quantum Dots. *J Chem Phys* **2019**, *151* (19), 194702. 10.1063/1.5126971.

(110) Koh, S.; Eom, T.; Kim, W. D.; Lee, K.; Lee, D.; Lee, Y. K.; Kim, H.; Bae, W. K.; Lee, D. C. Zinc–Phosphorus Complex Working as an Atomic Valve for Colloidal Growth of Monodisperse Indium Phosphide Quantum Dots. *Chemistry of Materials* **2017**, *29* (15), 6346–6355. 10.1021/acs.chemmater.7b01648.

(111) Kim, T.; Kim, S. W.; Kang, M.; Kim, S.-W. Large-Scale Synthesis of InPZnS Alloy Quantum Dots with Dodecanethiol as a Composition Controller. *J Phys Chem Lett* **2012**, *3* (2), 214–218. 10.1021/jz201605d.

(112) Toufanian, R.; Chern, M.; Kong, V. H.; Dennis, A. M. Engineering Brightness-Matched Indium Phosphide Quantum Dots. *Chemistry of Materials* **2021**, *33* (6), 1964–1975. 10.1021/acs.chemmater.0c03181.

(113) Nemoto, K.; Watanabe, J.; Sun, H.-T.; Shirahata, N. Coherent InP/ZnS Core@shell Quantum Dots with Narrow-Band Green Emissions. *Nanoscale* **2022**, *14* (27), 9900–9909. 10.1039/D2NR02071H.

(114) Kim, T.; Won, Y.-H.; Jang, E.; Kim, D. Negative Trion Auger Recombination in Highly Luminescent InP/ZnSe/ZnS Quantum Dots. *Nano Lett* **2021**, *21* (5), 2111–2116. 10.1021/acs.nanolett.0c04740.

(115) Sung, Y. M.; Kim, T.; Yun, D.; Lim, M.; Ko, D.; Jung, C.; Won, N.; Park, S.; Jeon, W. S.; Lee, H. S.; Kim, J.; Jun, S.; Sul, S.; Hwang, S. Increasing the Energy Gap between Band-Edge and Trap States Slows Down Picosecond Carrier Trapping in Highly Luminescent InP/ZnSe/ZnS Quantum Dots. *Small* **2021**, *17* (52), 2102792. 10.1002/smll.202102792.

(116) Nguyen, A. T.; Cavanaugh, P.; Plante, I. J.-L.; Ippen, C.; Ma, R.; Kelley, D. F. Auger Dynamics in InP/ZnSe/ZnS Quantum Dots Having Pure and Doped Shells. *The Journal of Physical Chemistry C* **2021**, *125* (28), 15405–15414. 10.1021/acs.jpcc.1c03015.

(117) Sun, H.; Cavanaugh, P.; Jen-La Plante, I.; Ippen, C.; Bautista, M.; Ma, R.; Kelley, D. F. Biexciton and Trion Dynamics in InP/ZnSe/ZnS Quantum Dots. *J Chem Phys* **2022**, *156* (5), 054703. 10.1063/5.0082223.

(118) Lim, J.; Bae, W. K.; Lee, D.; Nam, M. K.; Jung, J.; Lee, C.; Char, K.; Lee, S. InP@ZnSeS, Core@Composition Gradient Shell Quantum Dots with Enhanced Stability. *Chemistry of Materials* **2011**, *23* (20), 4459–4463. 10.1021/cm201550w.

(119) Lee, S. H.; Kim, Y.; Jang, H.; Min, J. H.; Oh, J.; Jang, E.; Kim, D. The Effects of Discrete and Gradient Mid-Shell Structures on the Photoluminescence of Single InP Quantum Dots. *Nanoscale* **2019**, *11* (48), 23251–23258. 10.1039/C9NR06847C.

(120) Lee, Y.; Jo, D.-Y.; Kim, T.; Jo, J.-H.; Park, J.; Yang, H.; Kim, D. Effectual Interface and Defect Engineering for Auger Recombination Suppression in Bright InP/ZnSeS/ZnS Quantum Dots. *ACS Appl Mater Interfaces* **2022**, *14* (10), 12479–12487. 10.1021/acsami.1c20088.

(121) Langof, L.; Ehrenfreund, E.; Lifshitz, E.; Micic, O. I.; Nozik, A. J. Continuous-Wave and Time-Resolved Optically Detected Magnetic Resonance Studies of Nonetched/Etched InP Nanocrystals. *J Phys Chem B* **2002**, *106* (7), 1606–1612. 10.1021/jp013720g.

(122) Blackburn, J. L.; Ellingson, R. J.; Mićić, O. I.; Nozik, A. J. Electron Relaxation in Colloidal InP Quantum Dots with Photogenerated Excitons or Chemically Injected Electrons. *J Phys Chem B* **2003**, *107* (1), 102–109. 10.1021/jp026746w.

(123) Fu, H.; Zunger, A. InP Quantum Dots: Electronic Structure, Surface Effects, and the Redshifted Emission. *Phys Rev B* **1997**, *56* (3), 1496–1508. 10.1103/PhysRevB.56.1496.

(124) Cho, E.; Kim, T.; Choi, S.; Jang, H.; Min, K.; Jang, E. Optical Characteristics of the Surface Defects in InP Colloidal Quantum Dots for Highly Efficient Light-Emitting Applications. *ACS Appl Nano Mater* **2018**, *1* (12), 7106–7114. 10.1021/acsanm.8b01947.

(125) Yang, W.; Yang, Y.; Kaledin, A. L.; He, S.; Jin, T.; McBride, J. R.; Lian, T. Surface Passivation Extends Single and Biexciton Lifetimes of InP Quantum Dots. *Chem Sci* **2020**, *11* (22), 5779–5789. 10.1039/D0SC01039A.

(126) Dümbgen, K. C.; Zito, J.; Infante, I.; Hens, Z. Shape, Electronic Structure, and Trap States in Indium Phosphide Quantum Dots. *Chemistry of Materials* **2021**, *33* (17), 6885–6896. 10.1021/acs.chemmater.1c01795.

(127) Cui, J.; Beyler, A. P.; Marshall, L. F.; Chen, O.; Harris, D. K.; Wanger, D. D.; Brokmann, X.; Bawendi, M. G. Direct Probe of Spectral Inhomogeneity Reveals Synthetic Tunability of Single-Nanocrystal Spectral Linewidths. *Nat Chem* **2013**, *5*, 602.

(128) Talapin, D. v. Experimental and Theoretical Studies on the Formation of Highly Luminescent II-VI, III-V and Core-Shell Semiconductor Nanocrystals. Ph.D. Dissertation, University of Hamburg, Germany, 2002.

(129) Brouwer, A. M. Standards for Photoluminescence Quantum Yield Measurements in Solution (IUPAC Technical Report). *Pure and Applied Chemistry* **2011**, *83* (12), 2213–2228. 10.1351/PAC-REP-10-09-31.

(130) Allen, M. W. Measurement of Fluorescence Quantum Yields. *Thermo Fisher Scientific* **2010**, *Technical Note* (52019).

(131) Dukes, A. D.; Samson, P. C.; Keene, J. D.; Davis, L. M.; Wikswo, J. P.; Rosenthal, S. J. Single-Nanocrystal Spectroscopy of White-Light-Emitting CdSe Nanocrystals. *J Phys Chem A* **2011**, *115* (16), 4076–4081. 10.1021/jp1109509.

(132) Schindelin, J.; Arganda-Carreras, I.; Frise, E.; Kaynig, V.; Longair, M.; Pietzsch, T.; Preibisch, S.; Rueden, C.; Saalfeld, S.; Schmid, B.; Tinevez, J.-Y.; White, D. J.; Hartenstein, V.; Eliceiri, K.; Tomancak, P.; Cardona, A. Fiji: An Open-Source Platform for Biological-Image Analysis. *Nat Methods* **2012**, *9* (7), 676–682. 10.1038/nmeth.2019.

(133) Byun, H.-J.; Song, W.-S.; Yang, H. Facile Consecutive Solvothermal Growth of Highly Fluorescent InP/ZnS Core/Shell Quantum Dots Using a Safer Phosphorus Source. *Nanotechnology* **2011**, *22* (23), 235605. 10.1088/0957-4484/22/23/235605.

(134) Bae, W. K.; Padilha, L. A.; Park, Y.-S.; McDaniel, H.; Robel, I.; Pietryga, J. M.; Klimov, V. I. Controlled Alloying of the Core–Shell Interface in CdSe/CdS Quantum Dots for Suppression of Auger Recombination. *ACS Nano* **2013**, *7* (4), 3411–3419. 10.1021/nn4002825.

(135) García-Santamaría, F.; Brovelli, S.; Viswanatha, R.; Hollingsworth, J. A.; Htoon, H.; Crooker, S. A.; Klimov, V. I. Breakdown of Volume Scaling in Auger Recombination in CdSe/CdS Heteronanocrystals: The Role of the Core−Shell Interface. *Nano Lett* **2011**, *11* (2), 687–693. 10.1021/nl103801e.

(136) Keene, J. D.; McBride, J. R.; Orfield, N. J.; Rosenthal, S. J. Elimination of Hole–Surface Overlap in Graded CdS x Se 1– x Nanocrystals Revealed by Ultrafast Fluorescence Upconversion Spectroscopy. *ACS Nano* **2014**, *8* (10), 10665–10673. 10.1021/nn504235w.

(137) Kippeny, T. C.; Bowers, M. J.; Dukes, A. D.; McBride, J. R.; Orndorff, R. L.; Garrett, M. D.; Rosenthal, S. J. Effects of Surface Passivation on the Exciton Dynamics of CdSe

Nanocrystals as Observed by Ultrafast Fluorescence Upconversion Spectroscopy. *J Chem Phys* **2008**, *128* (8), 084713. 10.1063/1.2834692.

(138) Garrett, M. D.; Dukes III, A. D.; McBride, J. R.; Smith, N. J.; Pennycook, S. J.; Rosenthal, S. J. Band Edge Recombination in CdSe, CdS and CdSx Se1−x Alloy Nanocrystals Observed by Ultrafast Fluorescence Upconversion: The Effect of Surface Trap States. *The Journal of Physical Chemistry C* **2008**, *112* (33), 12736–12746. 10.1021/jp803708r.

(139) Underwood, D. F.; Kippeny, T.; Rosenthal, S. J. Ultrafast Carrier Dynamics in CdSe Nanocrystals Determined by Femtosecond Fluorescence Upconversion Spectroscopy. *J Phys Chem B* **2001**, *105* (2), 436–443. 10.1021/jp003088b.

(140) Bowers II, M. J.; McBride, J. R.; Garrett, M. D.; Sammons, J. A.; Dukes III, A. D.; Schreuder, M. A.; Watt, T. L.; Lupini, A. R.; Pennycook, S. J.; Rosenthal, S. J. Structure and Ultrafast Dynamics of White-Light-Emitting CdSe Nanocrystals. *J Am Chem Soc* **2009**, *131* (16), 5730–5731. 10.1021/ja900529h.

(141) Garrett, M. D.; Bowers, M. J.; McBride, J. R.; Orndorff, R. L.; Pennycook, S. J.; Rosenthal, S. J. Band Edge Dynamics in CdSe Nanocrystals Observed by Ultrafast Fluorescence Upconversion. *The Journal of Physical Chemistry C* **2008**, *112* (2), 436–442. 10.1021/jp7099306.

(142) Biadala, L.; Siebers, B.; Beyazit, Y.; Tessier, Mickaël. D.; Dupont, D.; Hens, Z.; Yakovlev, D. R.; Bayer, M. Band-Edge Exciton Fine Structure and Recombination Dynamics in InP/ZnS Colloidal Nanocrystals. *ACS Nano* **2016**, *10* (3), 3356–3364. 10.1021/acsnano.5b07065.

(143) Ellingson, R. J.; Blackburn, J. L.; Yu, P.; Rumbles, G.; Mićić, O. I.; Nozik, A. J. Excitation Energy Dependent Efficiency of Charge Carrier Relaxation and Photoluminescence in Colloidal InP Quantum Dots. *J Phys Chem B* **2002**, *106* (32), 7758–7765. 10.1021/jp025666p.

(144) Freymeyer, N. J.; Click, S. M.; Reid, K. R.; Chisholm, M. F.; Bradsher, C. E.; McBride, J. R.; Rosenthal, S. J. Effect of Indium Alloying on the Charge Carrier Dynamics of Thick-Shell InP/ZnSe Quantum Dots. *J Chem Phys* **2020**, *152* (16), 161104. 10.1063/1.5145189.

(145) McBride, J.; Treadway, J.; Feldman, L. C.; Pennycook, S. J.; Rosenthal, S. J. Structural Basis for Near Unity Quantum Yield Core/Shell Nanostructures. *Nano Lett* **2006**, *6* (7), 1496–1501. 10.1021/nl060993k.

(146) Kahlow, M. A.; Jarzęba, W.; DuBruil, T. P.; Barbara, P. F. Ultrafast Emission Spectroscopy in the Ultraviolet by Time-gated Upconversion. *Review of Scientific Instruments* **1988**, *59* (7), 1098–1109. 10.1063/1.1139734.

(147) De, C. K.; Mandal, S.; Roy, D.; Ghosh, S.; Konar, A.; Mandal, P. K. Ultrafast Dynamics and Ultrasensitive Single-Particle Intermittency in Small-Sized Toxic Metal Free InP-Based Core/Alloy-Shell/Shell Quantum Dots: Excitation Wavelength Dependency Toward Variation of PLQY. *The Journal of Physical Chemistry C* **2019**, *123* (46), 28502–28510. 10.1021/acs.jpcc.9b09947.

(148) Rowland, C. E.; Liu, W.; Hannah, D. C.; Chan, M. K. Y.; Talapin, D. v.; Schaller, R. D. Thermal Stability of Colloidal InP Nanocrystals: Small Inorganic Ligands Boost High-Temperature Photoluminescence. *ACS Nano* **2014**, *8* (1), 977–985. 10.1021/nn405811p.

(149) Qidwai, A. A.; Woods, J. Defect Levels in Indium and Gallium Doped Zinc Selenide. *J Cryst Growth* **1982**, *59* (1), 217–222. https://doi.org/10.1016/0022-0248(82)90327-X.

(150) Hahm, D.; Chang, J. H.; Jeong, B. G.; Park, P.; Kim, J.; Lee, S.; Choi, J.; Kim, W. D.; Rhee, S.; Lim, J.; Lee, D. C.; Lee, C.; Char, K.; Bae, W. K. Design Principle for Bright, Robust, and Color-Pure InP/ZnSexS1–x/ZnS Heterostructures. *Chemistry of Materials* **2019**, *31* (9), 3476–3484. 10.1021/acs.chemmater.9b00740.

(151) Kovtun, O.; Tomlinson, I. D.; Ferguson, R. S.; Rosenthal, S. J. Quantum Dots Reveal Heterogeneous Membrane Diffusivity and Dynamic Surface Density Polarization of Dopamine Transporter. *PLoS One* **2019**, *14* (11), e0225339.

(152) Kovtun, O.; Torres, R.; Ferguson, R. S.; Josephs, T.; Rosenthal, S. J. Single Quantum Dot Tracking Unravels Agonist Effects on the Dopamine Receptor Dynamics. *Biochemistry* **2021**, *60* (13), 1031–1043. 10.1021/acs.biochem.0c00360.

(153) Brubaker, C. D.; Frecker, T. M.; McBride, J. R.; Reid, K. R.; Jennings, G. K.; Rosenthal, S. J.; Adams, D. E. Incorporation of Fluorescent Quantum Dots for 3D Printing and Additive Manufacturing Applications. *J Mater Chem C Mater* **2018**, *6* (28), 7584–7593. 10.1039/C8TC02024H.

(154) Makarov, N. S.; Korus, D.; Freppon, D.; Ramasamy, K.; Houck, D. W.; Velarde, A.; Parameswar, A.; Bergren, M. R.; McDaniel, H. Minimizing Scaling Losses in High-Performance Quantum Dot Luminescent Solar Concentrators for Large-Area Solar Windows. *ACS Appl Mater Interfaces* **2022**, *14* (26), 29679–29689. 10.1021/acsami.2c01350.

(155) Niezgoda, J. S.; Ng, A.; Poplawsky, J. D.; McBride, J. R.; Pennycook, S. J.; Rosenthal, S. J. Visualization of Current and Mapping of Elements in Quantum Dot Solar Cells. *Adv Funct Mater* **2016**, *26* (6), 895–902. 10.1002/adfm.201503839.

(156) Nguyen, H. A.; Sharp, D.; Fröch, J. E.; Cai, Y.-Y.; Wu, S.; Monahan, M.; Munley, C.; Manna, A.; Majumdar, A.; Kagan, C. R.; Cossairt, B. M. Deterministic Quantum Light Arrays from

Giant Silica-Shelled Quantum Dots. *ACS Appl Mater Interfaces* **2023**, *15* (3), 4294–4302. 10.1021/acsami.2c18475.

(157) Orfield, N. J.; McBride, J. R.; Keene, J. D.; Davis, L. M.; Rosenthal, S. J. Correlation of Atomic Structure and Photoluminescence of the Same Quantum Dot: Pinpointing Surface and Internal Defects That Inhibit Photoluminescence. *ACS Nano* **2015**, *9* (1), 831–839. 10.1021/nn506420w.

(158) McBride, J. R.; Mishra, N.; Click, S. M.; Orfield, N. J.; Wang, F.; Acharya, K.; Chisholm, M. F.; Htoon, H.; Rosenthal, S. J.; Hollingsworth, J. A. Role of Shell Composition and Morphology in Achieving Single-Emitter Photostability for Green-Emitting "Giant" Quantum Dots. *J Chem Phys* **2020**, *152* (12), 124713. 10.1063/5.0002772.

(159) Reid, K. R.; McBride, J. R.; la Croix, A. D.; Freymeyer, N. J.; Click, S. M.; Macdonald, J. E.; Rosenthal, S. J. Role of Surface Morphology on Exciton Recombination in Single Quantum Dot-in-Rods Revealed by Optical and Atomic Structure Correlation. *ACS Nano* **2018**, *12* (11), 11434–11445. 10.1021/acsnano.8b06472.

(160) Khlebtsov, B. N.; Khlebtsov, N. G. On the Measurement of Gold Nanoparticle Sizes by the Dynamic Light Scattering Method. *Colloid Journal* **2011**, *73* (1), 118–127. 10.1134/S1061933X11010078.

(161) Boyd, R. D.; Pichaimuthu, S. K.; Cuenat, A. New Approach to Inter-Technique Comparisons for Nanoparticle Size Measurements; Using Atomic Force Microscopy, Nanoparticle Tracking Analysis and Dynamic Light Scattering. *Colloids Surf A Physicochem Eng Asp* **2011**, *387* (1–3), 35–42. 10.1016/j.colsurfa.2011.07.020.

(162) Dorofeev, G. A.; Streletskii, A. N.; Povstugar, I. v.; Protasov, A. v.; Elsukov, E. P. Determination of Nanoparticle Sizes by X-Ray Diffraction. *Colloid Journal* **2012**, *74* (6), 675–685. 10.1134/S1061933X12060051.

(163) Pyrz, W. D.; Buttrey, D. J. Particle Size Determination Using TEM: A Discussion of Image Acquisition and Analysis for the Novice Microscopist. *Langmuir* **2008**, *24* (20), 11350–11360. 10.1021/la801367j.

(164) McBride, J. R.; Rosenthal, S. J. Real Colloidal Quantum Dot Structures Revealed by High Resolution Analytical Electron Microscopy. *J Chem Phys* **2019**, *151* (16), 160903. 10.1063/1.5128366.

(165) Wen, H.; Xu, X.; Cheong, S.; Lo, S.-C.; Chen, J.-H.; Chang, S. L. Y.; Dwyer, C. Metrology of Convex-Shaped Nanoparticles *via* Soft Classification Machine Learning of TEM Images. *Nanoscale Adv* **2021**, *3* (24), 6956–6964. 10.1039/D1NA00524C.

(166) Sun, Z.; Shi, J.; Wang, J.; Jiang, M.; Wang, Z.; Bai, X.; Wang, X. A Deep Learning-Based Framework for Automatic Analysis of the Nanoparticle Morphology in SEM/TEM Images. *Nanoscale* **2022**. 10.1039/D2NR01029A.

(167) Saaim, K. M.; Afridi, S. K.; Nisar, M.; Islam, S. In Search of Best Automated Model: Explaining Nanoparticle TEM Image Segmentation. *Ultramicroscopy* **2022**, *233*, 113437. 10.1016/j.ultramic.2021.113437.

(168) Lee, B.; Yoon, S.; Lee, J. W.; Kim, Y.; Chang, J.; Yun, J.; Ro, J. C.; Lee, J.-S.; Lee, J. H. Statistical Characterization of the Morphologies of Nanoparticles through Machine Learning Based Electron Microscopy Image Analysis. *ACS Nano* **2020**, *14* (12), 17125–17133. 10.1021/acsnano.0c06809.

(169) Yu, K.; Kelly, K. L.; Sakai, N.; Tatsuma, T. Morphologies and Surface Plasmon Resonance Properties of Monodisperse Bumpy Gold Nanoparticles. *Langmuir* **2008**, *24* (11), 5849–5854. 10.1021/la703903b.

(170) Periyasamy, M.; Kar, A. Modulating the Properties of SnO_2 Nanocrystals: Morphological Effects on Structural, Photoluminescence, Photocatalytic, Electrochemical and Gas Sensing Properties. *J Mater Chem C Mater* **2020**, *8* (14), 4604–4635. 10.1039/C9TC06469A.

(171) Gagner, J. E.; Lopez, M. D.; Dordick, J. S.; Siegel, R. W. Effect of Gold Nanoparticle Morphology on Adsorbed Protein Structure and Function. *Biomaterials* **2011**, *32* (29), 7241–7252. 10.1016/j.biomaterials.2011.05.091.

(172) Orfield, N. J.; McBride, J. R.; Wang, F.; Buck, M. R.; Keene, J. D.; Reid, K. R.; Htoon, H.; Hollingsworth, J. A.; Rosenthal, S. J. Quantum Yield Heterogeneity among Single Nonblinking Quantum Dots Revealed by Atomic Structure-Quantum Optics Correlation. *ACS Nano* **2016**, *10* (2), 1960–1968. 10.1021/acsnano.5b05876.

(173) Chang, H.; Kim, B. H.; Jeong, H. Y.; Moon, J. H.; Park, M.; Shin, K.; Chae, S. I.; Lee, J.; Kang, T.; Choi, B. K.; Yang, J.; Bootharaju, M. S.; Song, H.; An, S. H.; Park, K. M.; Oh, J. Y.; Lee, H.; Kim, M. S.; Park, J.; Hyeon, T. Molecular-Level Understanding of Continuous Growth from Iron-Oxo Clusters to Iron Oxide Nanoparticles. *J Am Chem Soc* **2019**, *141* (17), 7037–7045. 10.1021/jacs.9b01670.